ANNALS OF GEOPHYSICS, 69, 5, A546, 2026; doi:10.4401/ag-9525
OPEN ACCESS

A Comparative Study of Equatorial Ionospheric Irregularities Occurrence in the European/African Sector during the main phases of the 10-11 May 2024 and 10-11 October 2024 Geomagnetic Storms

Irina Zakharenkova[*,1,2], Iurii Cherniak[1,2], Andrzej Krankowski[1]

(1) University of Warmia and Mazury, Space Radio-Diagnostic Research Center, Olsztyn, Poland
(2) University Corporation for Atmospheric Research, COSMIC Program Office, Boulder, USA

Article history: received December 24, 2025; accepted June 19, 2026

Abstract

Two extreme geomagnetic storms occurred on 10-11 May 2024 and 10-11 October 2024. A prominent feature of both storms was the formation of the storm-induced equatorial plasma bubbles (EPBs), which extended largely from equatorial to mid-latitudes in the European/African longitudinal sector during the early stages of the storms. Using multi-instrument ground-based and satellite observations, we examined similarities and differences in the occurrence of the storm-induced ionospheric irregularities of equatorial origin over Europe. The formation of EPBs in the post-sunset sector was associated with storm-induced prompt penetration electric fields. The zonal extent of the storm-induced irregularities over the Mediterranean and northern African regions was closely tied to UT/LT difference for the sunset terminator location during the early stages of the storms. Ground-based GNSS ROTI maps showed intense ionospheric irregularities extending north and south from the magnetic equator, impacting northern Africa and southern Europe, in particular the Mediterranean region and the Iberian Peninsula, reaching latitudes as far north as 35°-40°N. Ground-based ionosondes in southern Europe detected strong spread-F conditions associated with the appearance of storm-induced EPBs. The scintillation observations from the INGV scintillation network provided clear evidence that strong amplitude scintillation events occurred in southern Europe during the main phases of the geomagnetic storms in May and October 2024. Intense ionospheric irregularities, associated with large-scale extension of storm-induced post-sunset EPBs, led to degradation of EGNOS performance in its European southern area.

Keywords: Ionospheric Irregularities; Geomagnetic Storm; Super Plasma Bubble; GNSS Scintillation; Mid-Latitude Ionosphere

1. Introduction

According to the International Solar Cycle Prediction Panel, the current solar cycle 25 reached its maximum in 2024. That year was also marked by two extreme geomagnetic storms happening on 10-11 May and 10-11 October 2024. The May 2024 storm, also known as the 2024 Mother's Day or Gannon storm, was the first storm with the geomagnetic three-hourly Kp index reaching its highest value of 9 since the famous "Halloween" storm in October 2003. These conditions correspond to an "extreme" G5 level of the National Oceanic and Atmospheric Administration Space Weather Prediction Center (NOAA SWPC) geomagnetic storm classification (https://www.swpc.noaa.gov/noaa-scales-explanation). Several years later, the May 2024 event is still considered as the most intense geomagnetic storm of the solar cycle 25, reaching a record low of −518 nT on the SYM-H index (the high-resolution version of the Dst index). This storm ranks among the most extreme in the past few decades (De Michelis and Consolini, 2025). This event is the subject of numerous published and ongoing studies on the Ionosphere-Thermosphere-Magnetosphere response to this outstanding geomagnetic storm, including registrations of storm-enhanced density and tongue-of-ionization structures in North America (Themens et al., 2024; Aa et al., 2024a), enormous strengthening of the equatorial ionization anomaly (EIA) due to super fountain effect at the daytime and dusk-side in the American sector (Singh et al., 2024; Fagundes et al., 2025; Zakharenkova et al., 2025a; Nayak et al., 2025), unusual merging of the southern EIA crest with the aurora near the southern tip of South America (Karan et al., 2024a), peculiar ionospheric enhancements at mid-latitudes in the Asian sector (Huang et al., 2024; Sun et al., 2024), significant negative ionospheric storm effects in the European sector (Spogli et al., 2024; Pierrard et al., 2025), and the rapid increase in thermospheric mass density that forced thousands of LEO satellites to perform orbit correction maneuvers (Parker and Linares, 2024). On 10-11 May 2024, the aurora borealis was visible at remarkably low latitudes, such as Japan, Korea, Italy, Namibia, South Africa, the USA, and Mexico (e.g. Hayakawa et al., 2025; Nanjo and Shiokawa, 2024; Kwak et al., 2024; Spogli et al., 2024; Gonzalez-Esparza et al., 2024; Hiyadutuje et al., 2025). The October 2024 event is considered as the second most powerful superstorm after the May 2024 event in the year 2024 and even in the solar cycle 25 (as of the year 2026). One of the first comparative analysis of ionospheric and plasmaspheric effects during these two storms was reported in Pierrard et al. (2025).

One of the most intriguing and least understood phenomena among various storm-driven ionospheric effects is the appearance of equatorial plasma bubbles (EPBs) that are being largely intensified by storm-induced electric fields. During geomagnetic storms, prompt penetrating electric fields (PPEFs) can immediately impact the equatorial ionosphere and the occurrence of regular post-sunset EPBs (e.g. Fejer et al., 1999; Huang, 2023). In the dusk sector, eastward-directed PPEFs can amplify the regular pre-reversal enhancement (PRE), resulting in a more dramatic development of EPBs due to much larger uplift of the ionosphere to higher altitudes where the Rayleigh-Taylor instability growth rate is maximized (e.g. Basu et al., 2001; Lee et al., 2006; Huang et al., 2024). The storm-driven uplift of the equatorial ionosphere can displace the storm-induced EPBs to locations far from the magnetic equator, occasionally reaching much higher altitudes and distant latitudes. Under geomagnetically quiet conditions, EPBs are typically constrained within the equatorial region, mainly between the northern and southern crest of the EIA, stretching up to 10-15° in latitude from the magnetic equator. Some geomagnetic storms can cause formation of extremely large EPBs, expanding up to 30-35° magnetic latitude (MLAT) from the magnetic equator to both hemispheres (e.g. Basu et al., 2005). Ma and Maruyama (2006) suggested to use the term "super plasma bubble" when they discovered one of the first observations of the post-sunset plasma bubbles reaching mid-latitudes of southern Japan (30°-34°N, 31° MLAT) during the February 2000 geomagnetic storm. In the present paper, we will refer the storm-induced EPBs with significant latitudinal extent (over 40°, beyond 20°N/S MLAT) as "super-bubbles", differentiating them from conventional EPBs.

During the last twenty years, more studies have been published on EPB detections at mid-latitudes amid geomagnetic storms of diverse intensity (e.g., Huang et al., 2007; Li et al., 2009, 2018; Martinis et al., 2015; Aa et al., 2018, 2019, 2024b, 2025; Cherniak and Zakharenkova, 2016, 2022; Cherniak et al., 2019; Zakharenkova and Cherniak, 2020, 2021; Zakharenkova et al., 2025b, 2025c; Rodrigues et al., 2021; Sousasantos et al., 2023; Sun et al., 2023, 2024; Karan et al., 2024b; Gomez Socola et al., 2025) – confirming that storm-induced super plasma bubbles can reach mid-latitudes more often than it was previously thought. The majority of these studies centered on the American and Asian longitudinal sectors. Reports of super plasma bubbles occurring in the European/African longitude sector are not numerous. Thus, Cherniak and Zakharenkova (2016) reported the first registration of the super plasma bubbles in southern Europe for the June 2015 geomagnetic storm using ground-based Global Navigation Satellite Systems (GNSS) measurements and in situ data of plasma density from Swarm and Defense

Meteorological Satellite Program (DMSP) satellites. Ionospheric irregularities were observed for more than 8 hours in the sector ~40-45°N (~35-40°N MLAT), ~0-35°E; they were connected to the plasma bite-out in the dusk sector over western African longitudes (Cherniak et al., 2019). Another research by Katamzi-Joseph et al. (2017) reported plasma depletions in ground-based GNSS and DMSP ion density observations as detected over southern Europe during the main phase of the April 2000 and 2001 geomagnetic storms. In a recent study by Campuzano et al. (2023), storm-induced ionospheric irregularities were again detected over the Iberian Peninsula using data from a digital ionosonde and several GNSS stations in Spain during two moderate storms, which occurred in February 2014 and September 2021. Appearing close to the maximum of the current solar cycle 25, the April 2023 storm produced extreme EPBs reaching mid-latitudes at ~40°N and ~30°S MLAT with apex altitudes of ~4,000 km at the magnetic equator over western African/Atlantic sector. The full latitudinal extent of these extreme bubbles was captured by the GOLD (Global-Scale Observations of the Limb and Disk) imager (Karan et al., 2024b; Aa et al., 2024b; Zakharenkova et al., 2025c). Despite this, the overall number of such cases for this longitudinal sector remains very low.

Interestingly, our analysis of ionospheric effects for these two extreme geomagnetic storms that took place in 2024 revealed that both storms appeared to trigger the development of highly intense ionospheric irregularities associated with the occurrence of super-EPBs in the European/African longitudinal sector. These EPBs extended far beyond equatorial latitudes reaching northern Africa and southern Europe. Given that the occurrence of storm-induced EPBs in southern Europe is a relatively rare phenomenon, the objective of this study is to examine similarities and differences between these events using a comprehensive set of satellite and ground-based observations.

2. Data and Methods

To study storm-induced ionospheric irregularities, we use the following observational data from several ground-based and satellite instruments:

1) Ground-based GNSS. We utilize measurements from 6,000+ ground-based GNSS stations worldwide to generate high-resolution maps of Rate Of TEC change Index (ROTI). TEC stands for the ionospheric Total Electron Content. ROTI expresses the sharpness of the GNSS signal phase fluctuations caused by ionospheric irregularities and by strong spatial gradients of the TEC. ROTI is calculated as a standard deviation of the time differential of TEC over 5 min (Aarons et al., 1997; Pi et al., 1997; Aarons and Lin, 1999). Details of the GNSS data processing and ROTI calculation were described by Zakharenkova et al. (2016) and Cherniak et al. (2014, 2018). For this study, we utilized GNSS signals provided by the GPS, GLONASS, Galileo, and BeiDou systems. The ROTI values were computed for each link between a ground-based receiver and a GNSS satellite with a 20° elevation angle cutoff to avoid multi-path effects at low elevations (e.g. Pi et al., 1997; Cherniak et al., 2014). Then, the multi-site ROTI values were binned into a geographic grid with (1.0°, 1.0°) spatial resolution to produce global ROTI maps at 5-min intervals.
2) COSMIC-2 (Constellation Observing System for Meteorology, Ionosphere, and Climate) in situ density measurements. COSMIC-2 mission with six satellites at a low inclination orbit was designed to study the equatorial ionosphere and atmosphere (Weiss et al., 2022). With more than six years in orbit, COSMIC-2 provides a remarkable dataset of equatorial ionosphere observations and EPB detections. The scientific payloads of the COSMIC-2 mission includes an Ion Velocity Meter (IVM) instrument (Heelis et al., 2017) to provide in situ ion density, composition, and temperature along the low inclination satellite orbits at ~530 km altitude, enabling simultaneous detection of EPBs across different local times/longitudinal sectors (Zakharenkova et al., 2023). Here, we used IVM total ion density (Ni) observations from COSMIC-2 “ivmLv2” Level-2 product.
3) Vertical sounding ionograms recorded by the El Arenosillo (37.1°N; 6.7°W; 27.6° MLAT) and Roquetes (40.8°N; 0.5°E; 33.1° MLAT) ionosondes in Spain, San Vito ionosonde (40.6°N; 17.8°E; 34.2° MLAT) in Italy, and Nicosia ionosonde (35.03°N; 33.16°E; 29.4° MLAT) in Cyprus.
4) Scintillation measurements from several specialized Septentrio PolaRx5S scintillation receivers in the European and African regions, provided though the electronic Space Weather upper atmosphere (eSWua, Upper Atmosphere and Radio Propagation Working Group, 2020) data portal managed by Istituto Nazionale di Geofisica e Vulcanologia (INGV).
5) EGNOS (European Geostationary Navigation Overlay Service) positioning accuracy performance reports.

3. Space Weather Conditions

Figure 1 presents geomagnetic conditions during 10-11 May and 10-11 October 2024; each two-day period includes the storm's main phase and starting of the recovery phase.

According to the International Service of Geomagnetic Indices at the Observatori de l'Ebre (https://www.obsebre.es/php/geomagnetisme/vrapides/ssc_2024_p.txt), the Sudden Storm Commencement (SSC) for the first storm was at 17:05 UT on 10 May 2024. The geomagnetic three-hourly Kp index immediately reached value of 8+ at 18 UT on 10 May 2024 and remained at a high level (8-9) until 15-18 UT on 11 May 2024 (Fig. 1c). This corresponds to an "extreme" G5 level of NOAA geomagnetic storm classification. The previous, pre-storm day of 9 May 2024 was very quiet with the daily sum of Kp values of ~10 only, whereas this value spiked to ~38 and ~67 for 10 and 11 May 2024, respectively. The interplanetary magnetic field (IMF) north-south component Bz was near zero level just before the SSC (Fig. 1a). After that, it rapidly turned southward, and remained mainly southward until ~19 UT, reaching a minimal value of −40.5 nT at 18:08 UT. During that time interval of 17-19 UT, the interplanetary electric field (IEF) dawn-to-dusk component Ey, potentially associated with penetration electric fields to low latitudes, was steady positive with a maximum value of ~20-28 mV/m (Fig. 1b). The next extended period of the steady southward IMF Bz was from 19:40 until 22:23 UT with the next minimum value of −40 nT at 21:50 UT. The auroral electrojet (AE) index increased rapidly to above 2000 nT after SSC, with some AE peaks exceeding 3000 nT observed between 19 and 20 UT on 10 May 2024 (Fig. 1c). Variations in the SYM-H index (the high-resolution version of the Dst index), representing the equatorial ring current's strength and therefore the intensity of a geomagnetic storm, is shown in Fig. 1d. During ~10 min in the storm's initial phase, the SYM-H rose rapidly from the background level of ~0-10 nT to +88 nT. After that, the SYM-H decreased rapidly in several stages, first to a minimum value of −183 nT at 19:21 UT with the estimated change rate of ~129 nT/hr, then to −354 nT at 23:12 UT, and the third stage was the index drop from −257 nT at 00:30 UT down to a minimum of −518 nT at 02:14 UT on 11 May 2024. Thus, this storm was characterized by a 9-hour-long main phase, beginning around 17 UT on 10 May and ending around 02 UT on 11 May 2024.

For the 10-11 October 2024 geomagnetic storm, the SSC was at 15:14 UT on 10 October 2024. The geomagnetic three-hourly Kp index rapidly raised to the value of 8- during 15-18 UT on 10 October 2024, remaining at a high

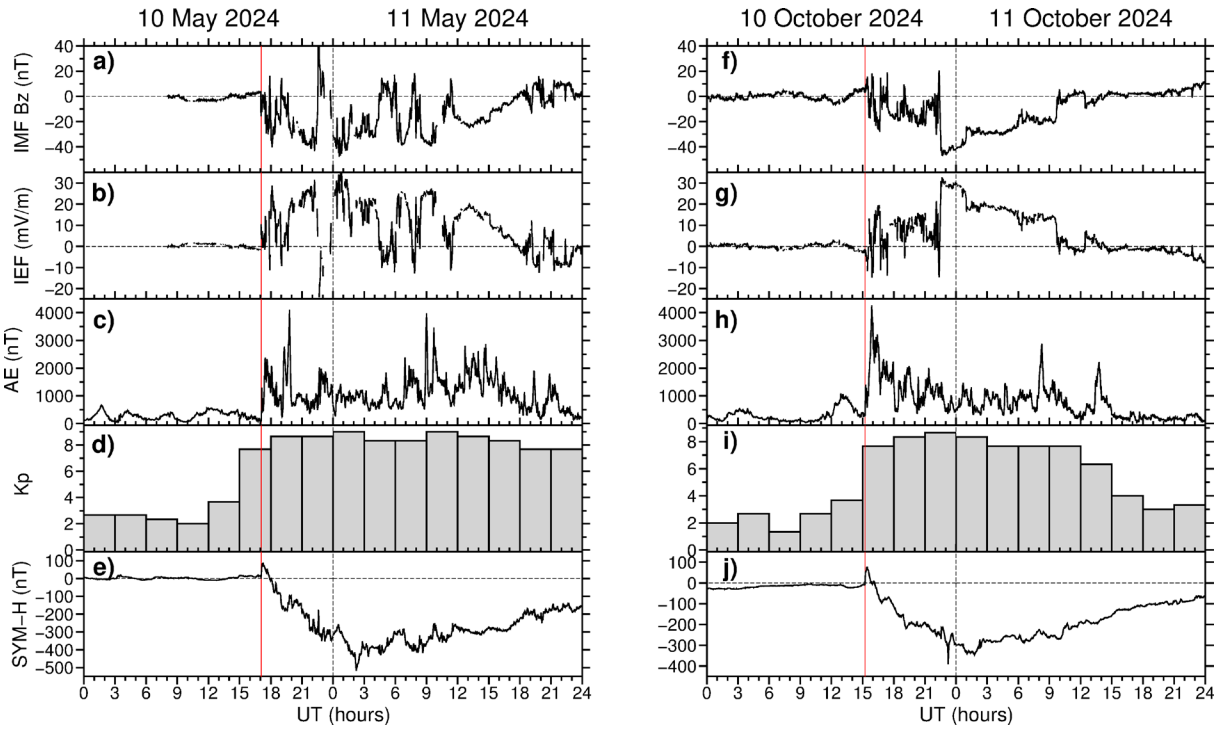

Figure 1. Geomagnetic conditions during 10-11 May and 10-11 October 2024: (a, f) Interplanetary Magnetic Field (IMF) Bz component, (b, g) Interplanetary Electric Field, (c, h) auroral electrojet AE index, (d, i) 3-hour Kp index, and (e, j) SYM-H index. The red vertical line shows the sudden storm commencement time.

level (~8) until 12 UT on 11 October 2024 (Fig. 1i). The largest registered Kp value was 9- during 21-24 UT on 10 October 2024. The IMF Bz was fluctuating near the zero level prior to the SSC (Fig. 1f). After that, there were several periods of southward IMF Bz in the range of −15-20 nT, each lasting 1-2 hours, during the storm's main phase. The IEF Ey was mostly positive during the main phase of the storm and beginning of the recovery phase (Fig. 1g). Immediately after the SSC, the AE index showed a very rapid rise to 3000-4000 nT near 16:00 UT, then the AE values dropped to the level of ~2000 nT during 17-18 UT and fluctuated between 500-1500 nT range during the rest part of the main phase (Fig. 1h). In the first 10 min into the storm's initial phase, the SYM-H rose quickly from the background level of −10-0 nT to +78 nT (Fig. 1j). After that, the SYM-H decreased rapidly in several steps, first to a minimum value of −65 nT at 16:49 UT, then to −220 nT at 19:11 UT, and finally to −346 nT at 01:46 UT on 11 October 2024, making a short-term excursion to −390 nT at 23:14 UT on 10 October 2024. This storm was characterized by a ~10-11-hour-long main phase, beginning after ~15 UT on 10 October and ending at ~02 UT on 11 October 2024. The start, end, and duration of the storm's main phase in terms of UT closely resembled the May 2024 geomagnetic storm.

4. Results

4.1 GNSS ROTI observations

We analyze the ground-based GNSS ROTI observations to geolocate areas affected by storm-induced ionospheric irregularities during the main phases of two geomagnetic storms in May and October 2024. Figure 2 presents a sequence of the GNSS ROTI maps centering on the European/African sector (15°E central meridian) for selected epochs on 10-11 May 2024. Data coverage is particularly good in the European region (35°-80°N latitude) because of the dense network of GNSS stations, whereas data gaps exist in the African region because of the sparse distribution of ground-based stations. Despite these gaps, the available coverage provides a rough spatial overview of the regions affected by intense ionospheric irregularities. The first ROTI map for 17:00 UT shows that the entire region is relatively quiet with absent or very weak ionospheric irregularities detected (dark-blue color, low ROTI < 0.3 TECU/min). As the storm developed, a progressive intensification of auroral irregularities (red color, ROTI > 0.8-1 TECU/min) is observed at high latitudes over northern Europe (above 60°N). The ROTI map for 17:30 UT shows the first signs of the post-sunset equatorial irregularities along the eastern coast of Africa. As the sunset terminator progressed to the west, the area affected by post-sunset irregularities extended into the western African sector. After 19:00-19:30 UT, the ionospheric irregularities started to expand towards northern Africa and southern Europe/Mediterranean zone. In the next hours, the zone with equatorial ionospheric irregularities, already reaching northern Africa and the Iberian Peninsula in southern Europe, continued its westward expansion, now including the Canary Islands (Spain) and the Azores and Madeira Islands (Portugal) in the Atlantic Ocean. The similar intensifications were also detected in the magnetically conjugate zone in the Southern Hemisphere over the Atlantic Ocean near the western coast of Africa (15°W-0°E). The zone affected by the post-sunset equatorial irregularities stretched between 20°S-40°N latitude and 30°W-40°E longitude. Near 22:30 UT, the high-latitude irregularities move further equatorward in the European sector, whereas in the opposite hemisphere they reach the southern part of South Africa, thus reducing the mid-latitudinal bands between the expanded zones of equatorial and auroral irregularities down to just 10-15° in latitude.

In a similar way, Fig. 3 shows the GNSS ROTI maps for 10-11 October 2024. Here, the geomagnetic storm's SSC was at 15:14 UT and a very high rise of the AE index up to ~4000 nT was observed at ~16 UT. Once the eastern African sector moved into the night-side after 16 UT, strong ionospheric irregularities were observed there, already expanded significantly in latitude, from 25°S to 35°N. At ~18-19 UT, the intense ionospheric irregularities were observed over nearly the entire African continent, spanning from northern Africa and the Mediterranean region down to southern Africa. In the Mediterranean zone, the irregularities affected Turkey, Greece and southern Italy, and after 20-21 UT the Iberian Peninsula. After ~23 UT, the intensity of the ionospheric irregularities detections started to diminish at low to mid-latitudes over the African sector. In the European part, the zone with intense high latitude irregularities expanded as far equatorward as 45°-50°N.

We further analyzed the longitudinal differences in the occurrence of ionospheric irregularities across Europe using the north-south cross-sections (keograms) derived from the GNSS ROTI maps along three different longitudes, 30°E, 15°E, and 5°W. Such keograms, plotted as a function of geographic latitude and UT time, show the averaged ROTI values across a narrow (±3.5°) band around the considered longitude. Figures 4a-4c present the GNSS ROTI

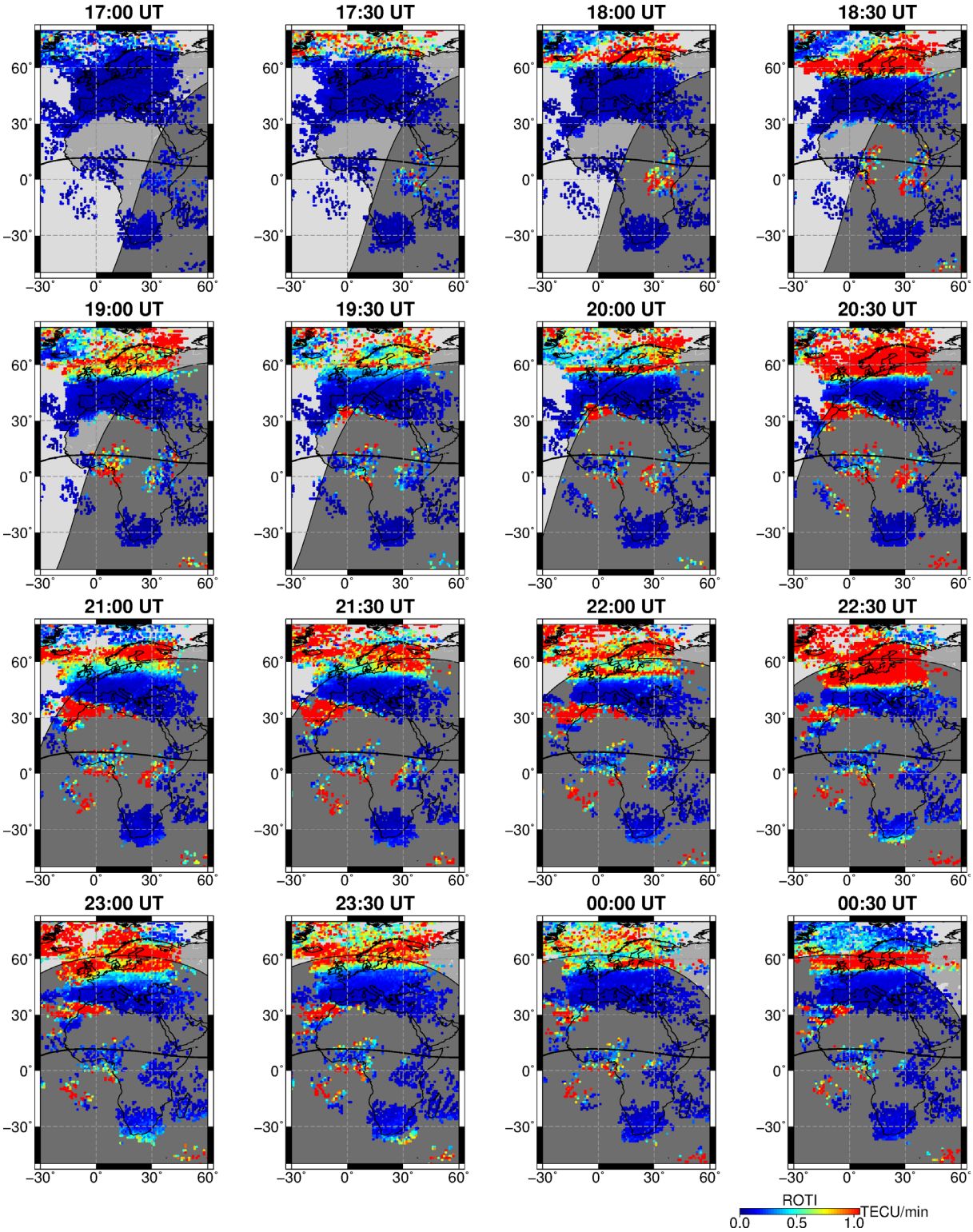

Figure 2. Ground-based GNSS ROTI observations in the European/African longitude sector during 17:00-00:30 UT on 10-11 May 2024. The dark grey shading indicates nighttime, and the black line shows the magnetic equator. High ROTI values (red color) show intense ionospheric irregularities, originating from equatorial and auroral regions.

keograms corresponding to different longitudes for 10-11 May 2024. Locations of the selected longitudes at eastern, central, and western parts of the Mediterranean area are shown as blue lines in Fig. 4g.

The first keogram in Fig. 4a illustrates GNSS ROTI observations along 30°E longitude, in the eastern Mediterranean region, near Turkey. We observed that signatures of high-latitude ionospheric irregularities began to intensify

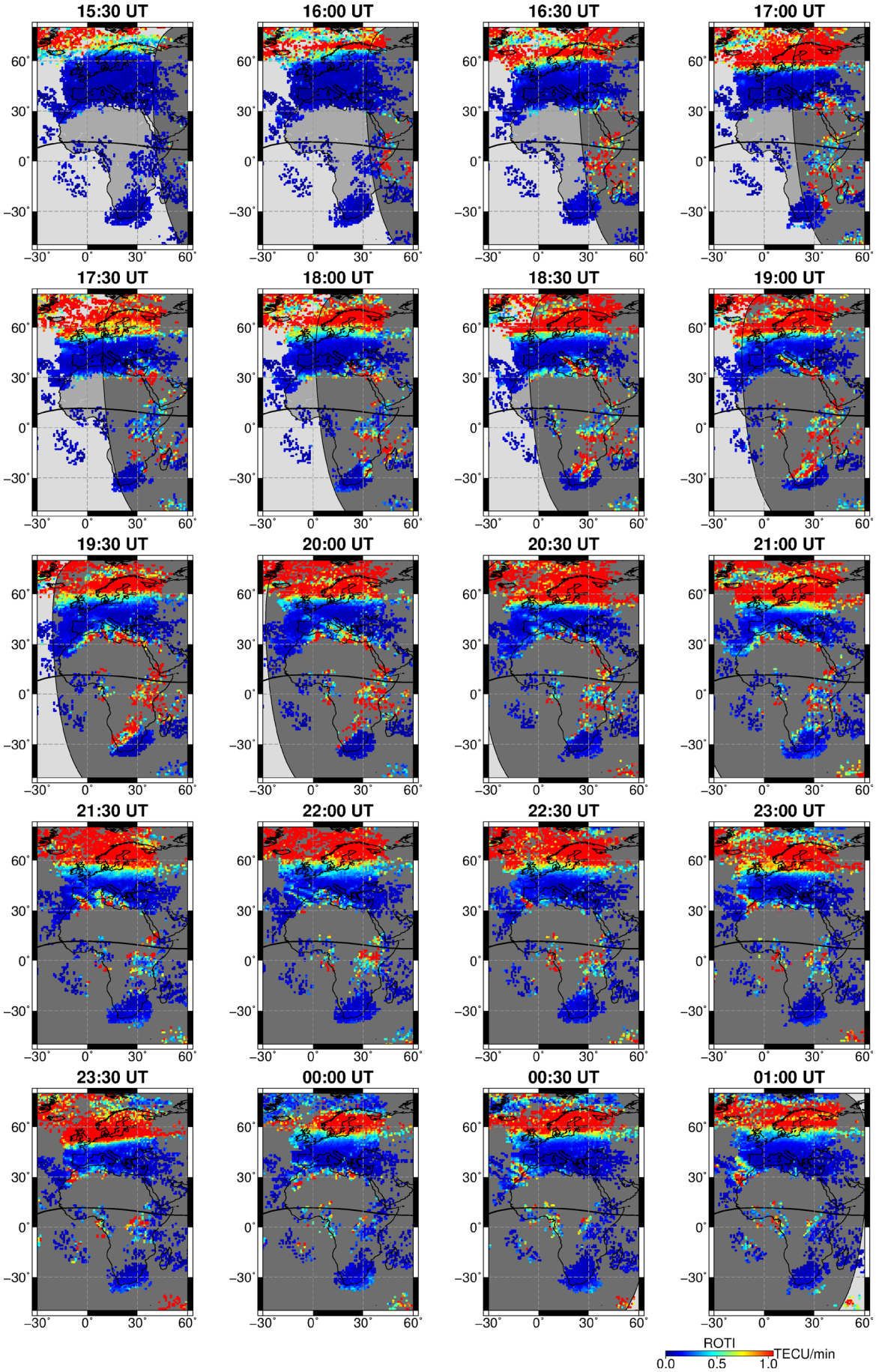

Figure 3. The same as Fig. 2 but for 15:30-01:00 UT on 10-11 October 2024.

and expanded equatorward after the SSC at ~17 UT. The high-latitude irregularities extended as far equatorward as ~55°N at ~19 UT and ~48°N at ~22-23 UT. In the southern zone, only very faint and sparse (partly due to limited data coverage) signatures of elevated ROTI values were detected near 25°N between 19 and 21 UT. Figure 4b shows the ROTI keogram for 15°E longitude, which crosses the central Mediterranean region near Italy. Here, the expansion patterns of high-latitude irregularities are very similar to those shown in Fig. 4a, while low-latitude irregularities became more apparent in this area, reaching 30°-35°N latitude between 18 and 23 UT. Further to the west, along 5°W longitude over the Iberian Peninsula (Fig. 4c), the ROTI keogram reveals low-latitude irregularities impacting a large zone over 25°-38°N, from 18 UT on 10 May to 02-03 UT on 11 May 2024. Therefore, for the May 2024 storm the most pronounced effects of low-latitude irregularities were detected mainly over the western and central parts of the Mediterranean region.

Figures 4d-4f display similar ROTI keograms at identical longitudes for the October 2024 storm. As the SSC occurred around 15 UT on 10 October 2024, high-latitude auroral irregularities began to expand equatorward after 15 UT, which is ~2 hr earlier than similar effects for the May 2024 storm. The high-latitude irregularities expanded as far equatorward as 50°-55°N, and they were observed from ~15 UT on 10 October to ~11 UT on 11 October 2024. Comparing low-latitude irregularities appearance along these three longitudes, the most affected zone was found near 30°E longitude, over the eastern Mediterranean region (Fig. 4d). Here, high ROTI values were estimated over 25°-35°N between ~16 UT and 22 UT. For the central Mediterranean region near 15°E (Fig. 4e), the elevated ROTI values were detected over 30°-40°N mainly between 18 and 22 UT, with some faint signatures lasting until ~03-04 UT

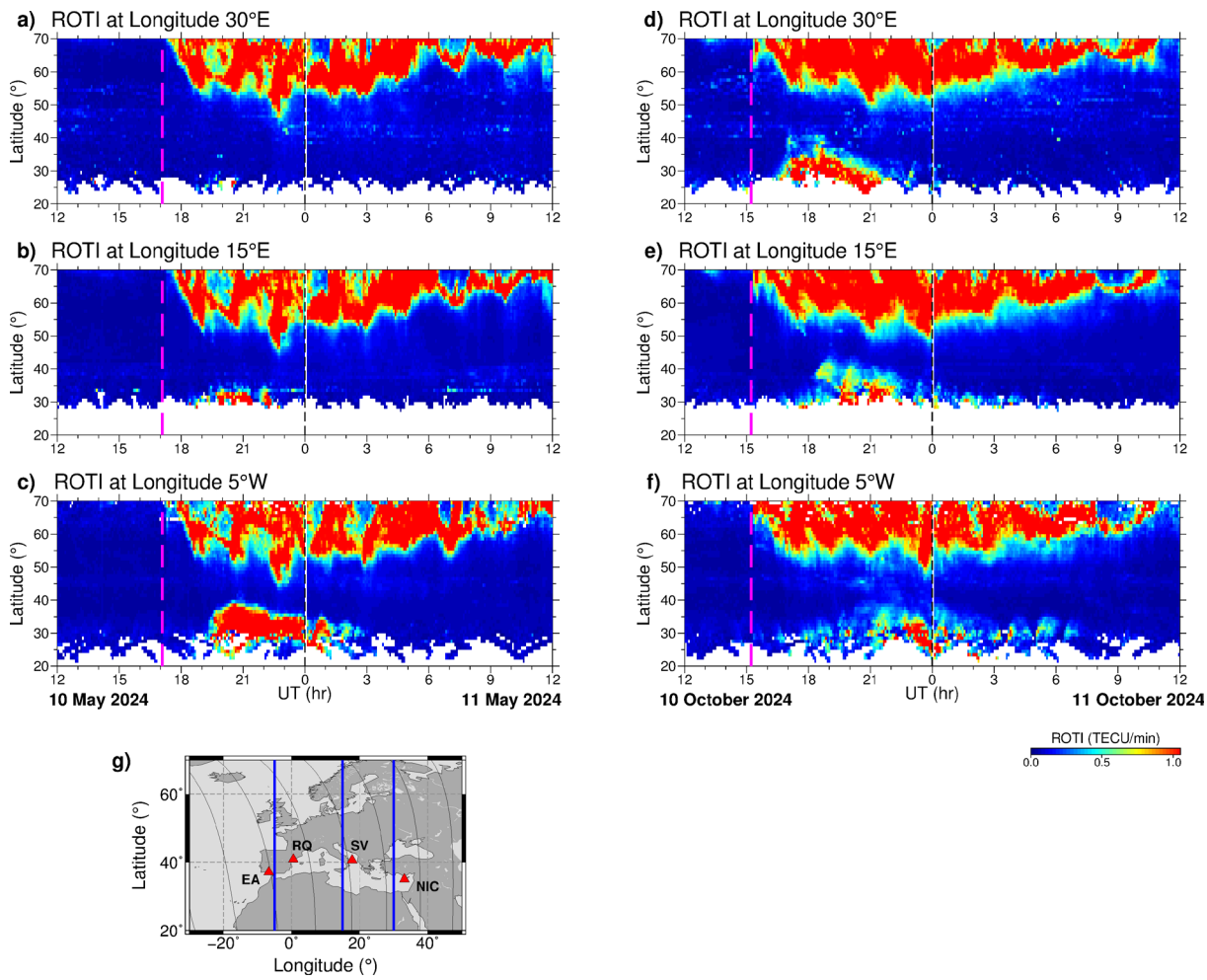

Figure 4. GNSS ROTI keograms representing spatio-temporal signatures of storm-induced ionospheric irregularities at three longitudes (30°E, 15°E, 5°W) on (a-c) 10-11 May and†(d-f) 10-11 October 2024. High ROTI values (red color) show intense ionospheric irregularities, originating from equatorial and auroral regions. The magenta vertical line shows the sudden storm commencement time. (g) Geographical map illustrating the locations of the selected longitudes for ROTI keograms (blue vertical lines), along with the ionosonde sites (red triangles).

on 11 October 2024. For the western Mediterranean area near 5°W (Fig. 4f), the ROTI keogram shows some signatures of low-latitude ionospheric irregularities from 18 UT on 10 October through 06 UT on 11 October 2024. The most intense irregularities, peaking between ~21 UT and 01 UT, occurred at latitudes of 25°-35°N in this region. Compared with the May 2024 storm, we note that due to an earlier storm onset, the storm-induced post-sunset irregularities occurred earlier in UT, when the night-time sector was still over more easterly longitudes, thus eastern and central Mediterranean zones were most affected.

4.2 COSMIC-2 IVM observations

It is clear that EPBs triggered by storm-induced electric fields might occur within a limited longitudinal zone. Finding actual limits of such longitudinal zone affected by the storm-induced EPBs can be difficult where ground-based observations are sparse, such as deserts and oceans. Here, LEO satellites equipped with in situ plasma probes can provide that critical information. Low inclination orbit satellites might be the best for this as their orbits revisit the entire equatorial and low latitude regions multiple times daily. For this study, we used in situ ion density observations from the COSMIC-2 mission, which consists of six satellites distributed evenly around the globe in a ~24° inclination orbit at ~530-550 km altitude (for the year 2024). Having six satellites in low-inclination orbits enables multiple satellite encounters within the specific sector per hour, facilitating the detection of plasma depletions by multiple satellites and offering data on their longitudinal differences.

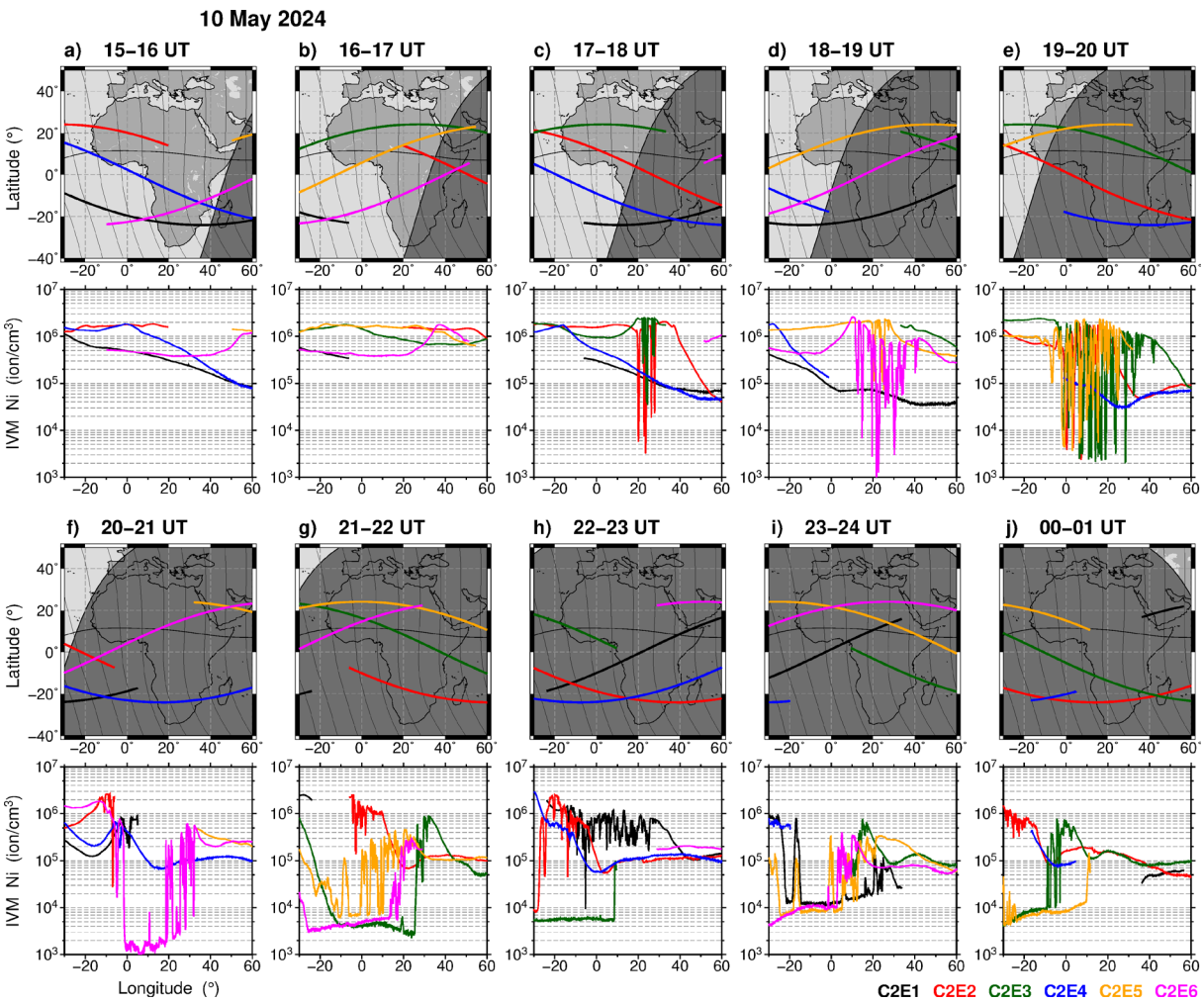

Figure 5. Sequence of maps for the African longitude sector with COSMIC-2 satellite tracks (C2E1-C2E6 marked by different colors) and in situ ion density measurements along these tracks for 1-hr intervals (a-j) during 15-01 UT on 10-11 May 2024. The thin black line on the maps marks the magnetic equator, the grey shading shows nighttime.

Figure 5 presents an overview of storm-induced plasma density depletions development in the European/African longitudinal sector as detected by COSMIC-2 IVM in situ density measurements during the evening time on 10-11 May 2024. Six COSMIC-2 satellites are marked here as C2E1 to C2E6. We can note that before the storm onset at ~17 UT, the first two maps constructed for 15-16 UT and 16-17 UT (Figs. 5a, 5b) show that there are mainly daytime conditions over the African sector, and several COSMIC-2 satellites with orbits over Africa detected very smooth ion density variations along these tracks. The next map in Fig. 5c shows the conditions for 17-18 UT, when the sunset is over eastern Africa and the geomagnetic storm just start to develop. Here, two satellites C2E2 and C2E3 (red and green lines in Fig. 5c) observe deep plasma density depletions, which are rapid drops in plasma density by several orders of magnitude, in the area around 20°-30°E longitudes. No post-sunset depletions are detected eastward of that zone over 40°-60°E. In the two following hours (Figs. 5d, 5e), COSMIC-2 observations show multiple plasma density depletion detections over the central region of Africa with intense plasma density depletions extend further west (following the sunset terminator), now covering a longitudinal range of 0°-40°E. Figure 5f shows the situation for 20-21 UT, when the entire African continent is under post-sunset conditions. The storm has already been developing for several hours, with a steady southward IMF Bz (Fig. 1a). Here, C2E6 satellite crosses the magnetic equator area and detects a broad plasma bite-out over 0°-30°E longitudes. The huge, broad plasma bite-outs are detected by several satellites further westward between 20°W and 10°-30°E during 21-01 UT (Figs. 5g-5j).

Figure 6 presents COSMIC-2 IVM in situ density measurements during 15-01 UT on 10-11 October 2024. Before the storm onset at 15:14 UT, the first map for 15-16 UT (Fig. 6a) showed very smooth ion density variations along satellite tracks. One hour later at 16-17 UT (Fig. 6b), when the sunset reached eastern Africa, three satellites (C2E1, C2E5 and C2E6) encountered very intense plasma density depletions both south and north of the magnetic equator between 30° and 60°E longitudes. In the next few hours (Figs. 6c-6e), following the sunset terminator

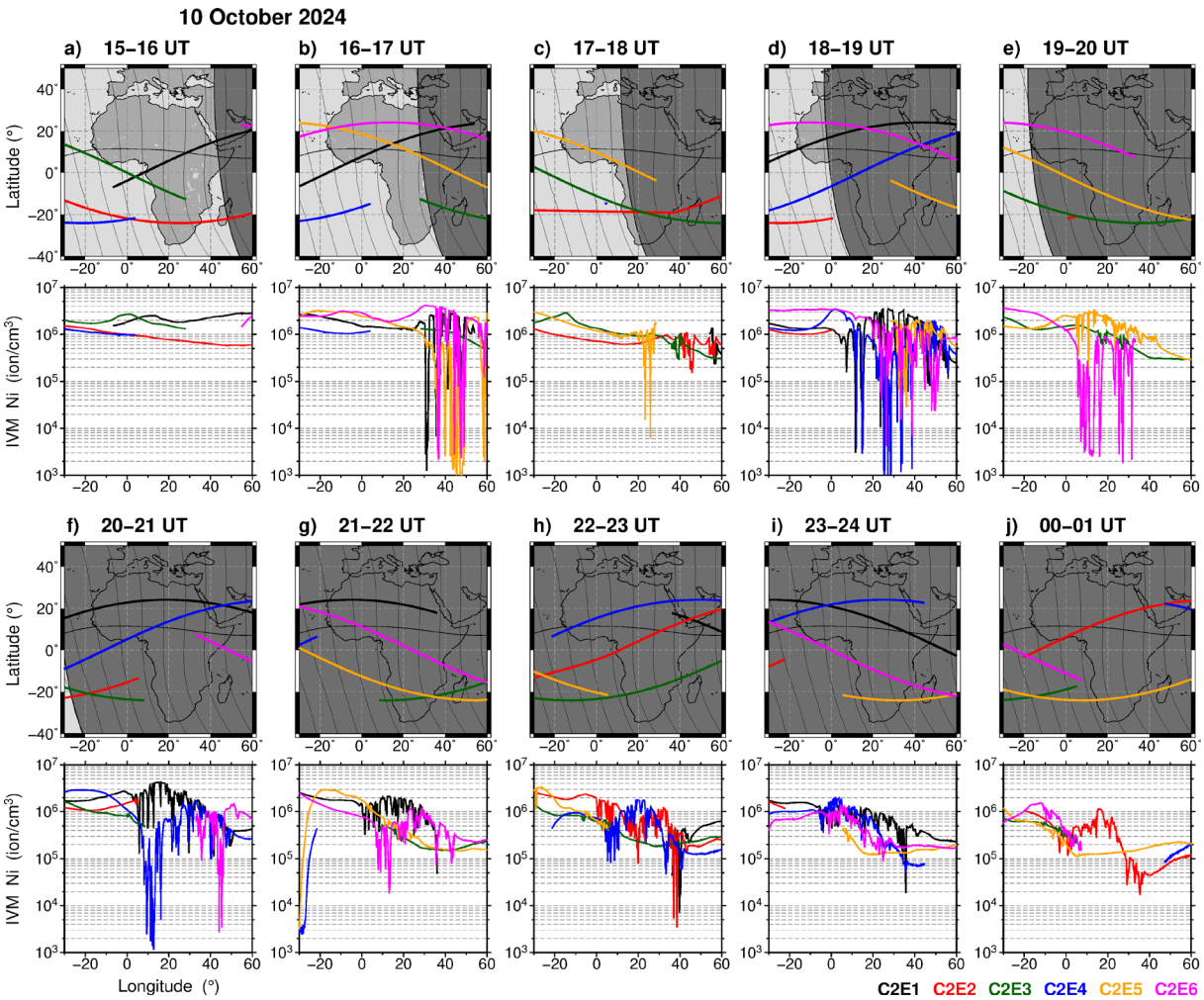

Figure 6. The same as Fig. 5 but for 10-11 October 2024.

progression, the plasma depletions occurred further westward over the central part of the African continent. During 20-01 UT (Figs. 6f-6j), the plasma density detections were mainly confined over the African region between 0°E and 40°E longitudes. No broad plasma bite-outs were observed here during the October 2024 storm.

4.3 Ionosonde observations

For many decades, the High Frequency (HF) sounding radars – ionosondes – provide unique opportunities to observe so called equatorial spread-F reflections associated with EPB development over the stations located in low latitudes. We investigated the occurrence of spread-F reflections, which indicate the storm-induced ionospheric irregularities development, using several ionosondes across the European Mediterranean region (ionosondes are marked as red triangles on the map in Fig. 4g). Here, we examined available ionograms from three stations for the case of May 2024 geomagnetic storm and for four stations for the October 2024 geomagnetic storm event. The raw ionograms from all of these stations are publicly available via the Global Ionospheric Radio Observatory (GIRO; more details in Reinisch and Galkin, 2011) Digital Ionogram DataBase (DIDbase, permanent web link is: https://giro.uml.edu/didbase/). Fundamentally, HF digisondes provide records of ionograms in virtual height (h′, km) of HF reflections from a particular ionospheric layer with plasma frequency (f, MHz) directly depended on plasma density at this layer. From the ionograms, one can derive peak parameters (height and density) of the ionospheric layers (E, F1, F2) and vertical electron density profiles Ne(h) can be inverted through specific procedures such as a true height inversion analysis, for example the Automated Real Time Ionogram Scaler and True height (ARTIST) in automatic or manual (expert) mode (Reinisch and Galkin, 2011).

As we mentioned above, HF radio waves are reflected from a specific ionospheric layer and most often they are recorded as sharp, well-defined lines with clear virtual height and frequency reflection. However, in a highly structured ionosphere, such as in the presence of well-developed EPBs, these reflections can diffuse or spread over a broad range of frequencies, heights, or both, and are classified as spread-F reflections. We then examined the ionograms from the available stations to identify such spread-F signatures, which may be associated with storm-induced EPBs and low-latitude ionospheric irregularities over southern Europe.

Figure 7 presents series of ionograms, recorded at 30-minute intervals during the evening on 10-11 May 2024, by three digisonde stations El Arenosillo and Roquetes Ebre in Spain, and San Vito in Italy. For the El Arenosillo ionosonde (Fig. 7a), the ionograms from 18:00 until 19:30 UT showed clear reflections with the F2 layer critical frequency (foF2) being near 8-9 MHz. Starting from ~20 UT, the ionograms appeared affected by diffusive reflections at frequency and height (mixed spread-F type). Such spread-F reflections are not frequently observed at mid-latitudes. Typically, such reflections can be detected at mid-latitude stations located further poleward during geomagnetic storms disturbances, caused by particles precipitations and auroral structures expanding equatorward from high to mid-latitudes. At the El Arenosillo station, spread-F on the ionograms persisted for ~4 hours from 20 UT on 10 May 2024 until midnight. Afterward, spread-F signatures disappeared at the background of a decrease in F-layer density (to ~2-3 MHz) and an uplift of the layer above 600 km height (during 0:30-2:30 UT on 11 May 2024). The ionosonde records for the Roquetes Ebre station (Fig. 7b), another station in Spain, showed mainly clear ionograms without spread-F signatures between ~18 UT and 20 UT and the critical frequency foF2 was near 8-9 MHz, similar to such observations at the El Arenosillo station during this period. Some signatures of diffusive reflections appeared at 20:30 UT on 10 May 2024; however, they were mainly due to oblique reflections. After midnight, here we also note the F2 layer density decrease (to 2-3 MHz) and the F2 layer uplift. At that time, some weak spread-F signatures became visible on the ionograms and were observed at least until 05 UT on 11 May 2024. For the San Vito station (Fig. 7c), located more eastward in Italy, the ionograms showed rather clear reflections from 18 UT until 23 UT on 10 May 2024. After ~23 UT, the F2 layer was uplifted to a higher altitude, showing plasma density decrease (foF2 dropped to 2-3 MHz). Frequency spread-F appeared near the critical frequency reflections on these ionograms and lasted until ~03 UT on 11 May 2024. Therefore, for the May 2024 storm, the most pronounced spread-F effects in the post-sunset sector were detected only at the southern Spain station El Arenosillo.

Figure 8 shows the ionosonde observations in the similar way for the 10-11 October 2024 event, but here observations from the Nicosia station located on Cyprus in eastern Mediterranean region became available too. Figure 8a demonstrated that at the most westward ionosonde, El Arenosillo at 6.7°W longitude, the ionograms were clear until ~21:30 UT; then, the range spread-F started to appear at the ionograms. At ~23 UT, the F2 layer rapidly uplifted and the later ionograms were affected by frequency spread-F reflections until at least 02 UT on

11 October 2024. At the Roquetes Ebre station, located eastward (0.5°E), the spread-F was observed earlier, starting at ~20 UT and continuing until ~23 UT; the significant F2 layer uplift occurred near 23 UT pushing all F2 layer reflections to virtual heights above 600-700 km for several hours (Fig. 8b). At the San Vito ionosonde (Fig. 8c), which is located at 17.8°E longitude in Italy and should observe sunset at earlier hours, the spread-F signatures appeared after 18:30 UT and persisted until ~22 UT. For the most eastward station, Nicosia located at 33.1°E longitude in Cyprus, Fig. 8d shows ionograms for the temporal interval of 16:00 UT-0:30 UT on 10-11 October 2024. The storm onset was at ~15 UT and the first strong spread-F signature started to appear here after 17 UT, which is ~19 LT in this sector. The spread-F signatures persisted for ~5 hours from 17:00 UT until 21:30 UT.

There are some similarities and differences of the spread-F signatures detected over longitudinally distanced ionosondes in southern Europe. First, for both cases of the extreme geomagnetic storms in May and October 2024, the spread-F conditions were observed in the post-sunset period in southern Europe. For the May 2024 event started at ~17 UT on 10 May 2024, the most pronounced signatures were observed at the western ionosonde El Arenosillo at 6.7°W longitude. For the October 2024 event with the earlier storm onset at ~15 UT, the spread-F conditions in the post-sunset period were detected at all ionosondes from El Arenosillo at 6.7°W longitude to Nicosia at 33.1°E longitude, meaning that storm-induced irregularities affected a broader range of longitudes in the European/African sector. Also, for the October 2024 event, we saw that spread-F detections were observed consecutively at different UT time when the sunset terminator moved from eastern to western Mediterranean region and the starting time corresponded roughly to 19-20 LT at the used stations.

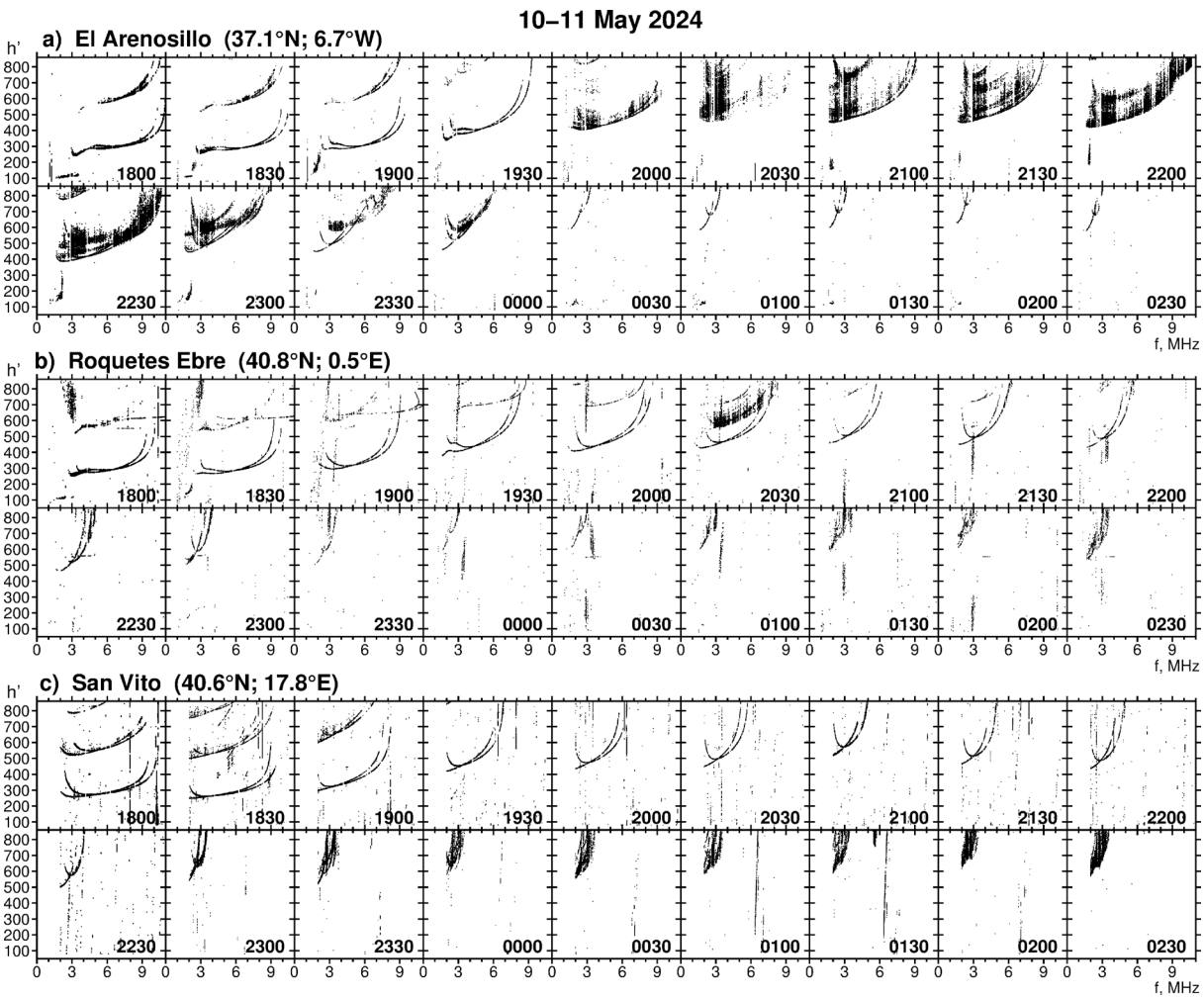

Figure 7. Sequence of vertical ionograms (virtual height in km vs. frequency in MHz) recorded during 18:00-02:30 UT on 10-11 May 2024 by (a) El Arenosillo digisonde (37.1°N; 6.7°W; 27.3° magnetic latitude), (b) Roquettes Ebre digisonde (40.8°N; 0.5°E; 33.1° magnetic latitude), (c) San Vito digisonde (40.6°N; 17.8°E; 34.2° magnetic latitude). The diffuse echoes correspond to spread-F conditions.

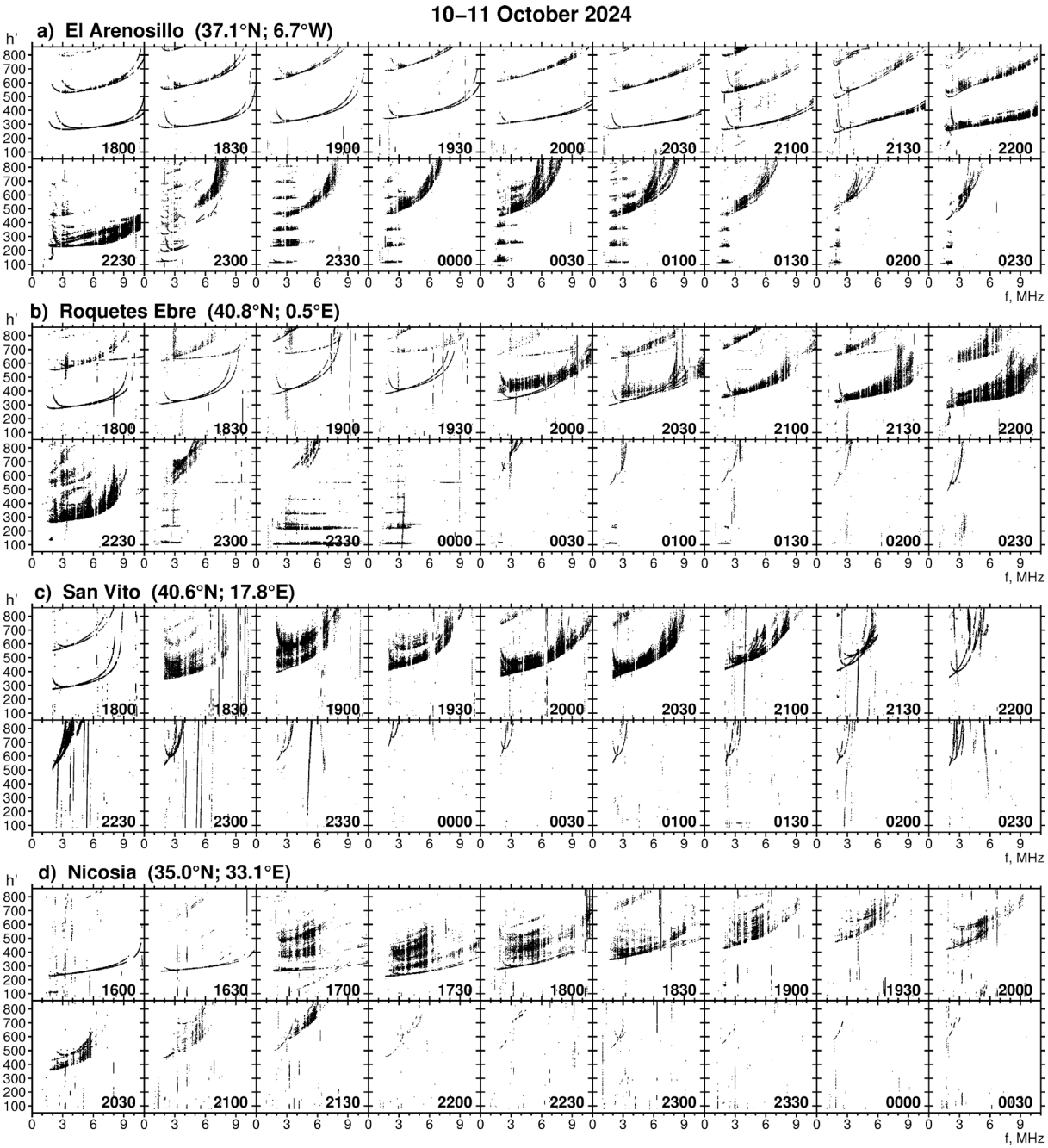

Figure 8. ≠Sequence of vertical ionograms (virtual height in km vs. frequency in MHz) recorded during 18:00-02:30 UT on 10-11 October 2024 by (a) El Arenosillo digisonde (37.1°N; 6.7°W; 27.3° magnetic latitude), (b) Roquettes Ebre digisonde (40.8°N; 0.5°E; 33.1° magnetic latitude), (c) San Vito digisonde (40.6°N; 17.8°E; 34.2° magnetic latitude), and (d) during 16:00-00:30 UT by Nicosia digisonde (35.0°N; 33.1°E; 29.3° magnetic latitude). The diffuse echoes correspond to spread-F conditions.

The ionospheric observations from the longitudinally distributed ionosondes provide observational evidence of the occurrence of unusual ionospheric irregularities over southern European latitudes and it allows us to see dynamics and evolution of these structures with the geomagnetic storm progression.

4.4 Scintillation observations

Besides GNSS ROTI observations, which are often considered as a proxy of phase scintillation, we have analyzed amplitude scintillation measurements provided by several Septentrio PolaRx5S scintillation receivers located

in the European and African regions. The scintillation data is available at the electronic Space Weather upper atmosphere (*eSWua*, http://www.eswua.ingv.it/) data portal managed by INGV (Upper Atmosphere and Radio Propagation Working Group, 2020). The commonly used scintillation indices for measuring the amplitude and phase scintillation are S4 and σ_φ (sigma_phi), respectively (Fremouw et al., 1978; Basu et al., 1985). The S4 index is the standard deviation of the received power normalized by its mean value, and the phase scintillation index is the standard deviation of the detrended carrier-phase measurements.

Amplitude (S4) scintillation data collected from Septentrio PolaRx5S scintillation receivers during both geomagnetic storms is featured in Fig. 9. Panels (a-c), shows data from three stations during 10-11 May 2024. Panels (d-h) present data from five stations during 10-11 October 2024. Panel (i) provides a geographical map illustrating the locations of the utilized stations. The scintillation indices were computed using samples measured at 50 Hz rates for intervals of 60 s. Similar to the GNSS ROTI analysis, we used an elevation angle cut-off of 20°. For the first event in May 2024, the GNSS scintillation records were available from the three stations – Lampedusa (35.52°N, 12.63°E; 26.8° MLAT) in Italy, Chania (35.52°N, 24.04°E; 28.6° MLAT) in Greece, and Abuja (8.99°N, 7.38°E; –2.2° MLAT) in Nigeria. Between 19 and 22 UT on the evening of 10 May 2024, Lampedusa station detected a significant rise in scintillation activity, with S4 values reaching 0.5-1.0 (Fig. 9a). The Chania station (Fig. 9b) also showed elevated S4 detections near 19-21 UT, however less significant than those of Lampedusa station. At the equatorial station Abuja (Fig. 9c), an increase in scintillation activity was detected at ~18:30 UT on 10 May 2024 and it continued for several hours, but the magnitude of amplitude scintillation (~0.5) was much smaller than the effects observed at the stations in the Mediterranean region. It is known that EPBs typically cause stronger scintillation in the EIA crest's region (larger background density and DN/N ratio) than directly over the magnetic equator. For the second storm event in October 2024, the scintillation records were available from two additional stations – Nicosia (35.18°N, 33.38°E; 29.6° MLAT) in Cyprus and Nairobi (1.29°S, 36.80°E; –9.0° MLAT) in Kenya. At Lampedusa station (Fig. 9d),

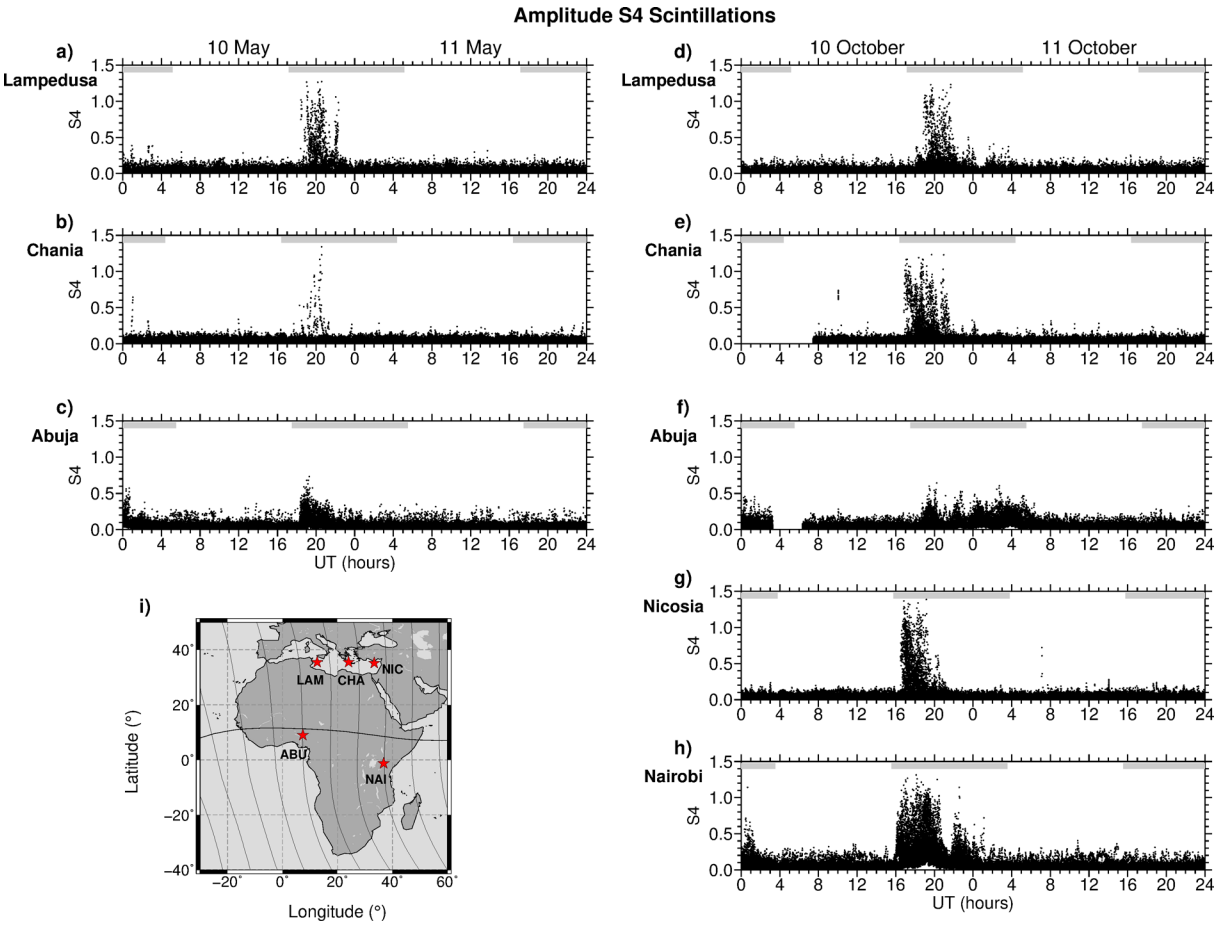

Figure 9. Time series of amplitude S4 scintillation observations at L1 frequency as recorded by GNSS scintillation receivers in Europe and Africa for (a-c) 10-11 May and (d-h) 10-11 October 2024; grey bars at the top shows night-time conditions of 18-06 LT. (i) Geographical map illustrating the scintillation receiver positions.

amplitude scintillation intensified, with S4 values reaching 0.5-1.0, between 19 and 22 UT on 10 October 2024 – very similar to the observations during the 10-11 May 2024 storm. This time at the Chania station at 24.0°E longitude in Greece (Fig. 9e), strong amplitude scintillation occurred between 17 UT and 21 UT. At the most eastern station in Nicosia at 33.4°E longitude in Cyprus (Fig. 9g), the strong scintillation event with S4 > 0.8 was observed during 17-20 UT. In the African region, one can see some moderate intensification of amplitude scintillation (S4 up to 0.3-0.5) at the western station Abuja at 7.4°E longitude, whereas the eastern station Nairobi at 36.8°E longitude showed a much stronger increase in scintillation (S4 up to 0.5-1.0) during 16-21 UT. Observations from the Nairobi station show a good agreement in time and magnitude of intense amplitude scintillation with corresponding observations at the northern stations Chania and Nicosia located in the European Mediterranean region. Near-simultaneous observations of strong amplitude scintillation at Nicosia and Nairobi suggests that both stations might be within the same region impacted by EPB structures extending from the equatorial zone to the European Mediterranean area, which can be also recognized in the GNSS ROTI maps for 19-20 UT in Fig. 3. This occurrence of intense amplitude scintillation at Nicosia was detected simultaneously with spread-F echo detections by the ground-based ionosonde at Nicosia (Fig. 8d).

These results provide clear observational evidence that strong amplitude scintillation events were detected from the ground in southern Europe during the main phases of the geomagnetic storms in May 2024 and October 2024. We should emphasize that the occurrence of strong amplitude scintillation in mid-latitudes, notably at equatorward-facing azimuths, is frequently associated to storm-intensified EPBs (e.g. Rodrigues et al., 2021; Sousasantos et al., 2023; Gomez Socola et al., 2025), including the examined case with the intense amplitude scintillation at Lampedusa station during the 10-11 May 2024 storm (Spogli et al., 2024).

4.5 EGNOS

In the previous sections, we described observations of scintillation-causing ionospheric irregularities of equatorial origin, which represent a rare phenomenon occurred in southern Europe during the main phases of the two extreme geomagnetic storms. The storm-induced EPBs that reach European mid-latitudes can seriously affect the performance of ground-based systems that rely on transionospheric radio wave propagation, particularly GNSS-based systems. In this section, we analyze the performance degradation of the European Geostationary Navigation Overlay Service (EGNOS). EGNOS is used to augment GNSS navigation constellations for the safety-critical applications such as aircrafts flying and landing assistance, supporting of near coast and narrow channels marine navigation, unmanned aerial systems, railways, precise agriculture, emergency calls, etc (EGNOS SoL SDD, 2024).

One of the EGNOS goals is to allow users of this system in Europe to determine their position with an accuracy within 1.5 m, but in the presence of strong ionospheric disturbances such as ionospheric plasma density irregularities and plasma density gradients, the performance of this system can be degraded significantly. The initial configuration of the EGNOS ground-based segment includes 34 Ranging Integrity Monitoring Stations (RIMS) located over a wide geographical area. The primary function of the RIMS is to collect measurements from GPS satellites and transmit raw data every second to the Central Processing Facilities (CPF). Figure 10 presents daily summary status plots with Horizontal and Vertical Navigation System Errors (HNSE and VNSE, respectively) for each RIMS site for 10 and 11 May 2024. The Navigation System Errors (NSE) should be understood as the difference between the true position and the estimated position, and the presented figures include the 95th percentile of this NSE (represented by the color scale) and the standard deviation of the NSE distribution (represented by the size of the circles) at every RIMS. During geomagnetically quiet days, most EGNOS RIMS sites usually have daily HNSE and VNSE positioning errors within 0.7-1.4 m, which are typically represented as small, green circles on such daily summary plots. On the first day of the storm (10 May 2024) and the next day (11 May 2024), both HNSE and VNSE parameters significantly increased from the nominal level to above 4 m (saturated scale on the plots) for RIMS located in the western Mediterranean region (Spain and Portugal) and northern Africa. Here, most EGNOS RIMS showing degraded performance were located in the southern part of the system (25°-40°N), whereas such degradation is typically expected at northernmost (high-latitude) RIMS due to effects of storm-time auroral irregularities.

Figure 11 shows similar EGNOS performance summary plots for 10-11 October 2024. We can note very significant performance degradation, especially in terms of the vertical errors, at the northern high-latitude RIMS sites on 10 October 2024. Strong degradation was also observed at the southern RIMS, similar to the May 2024 storm, however, this time more stations were affected in the southern and southeastern parts of the EGNOS service area, including

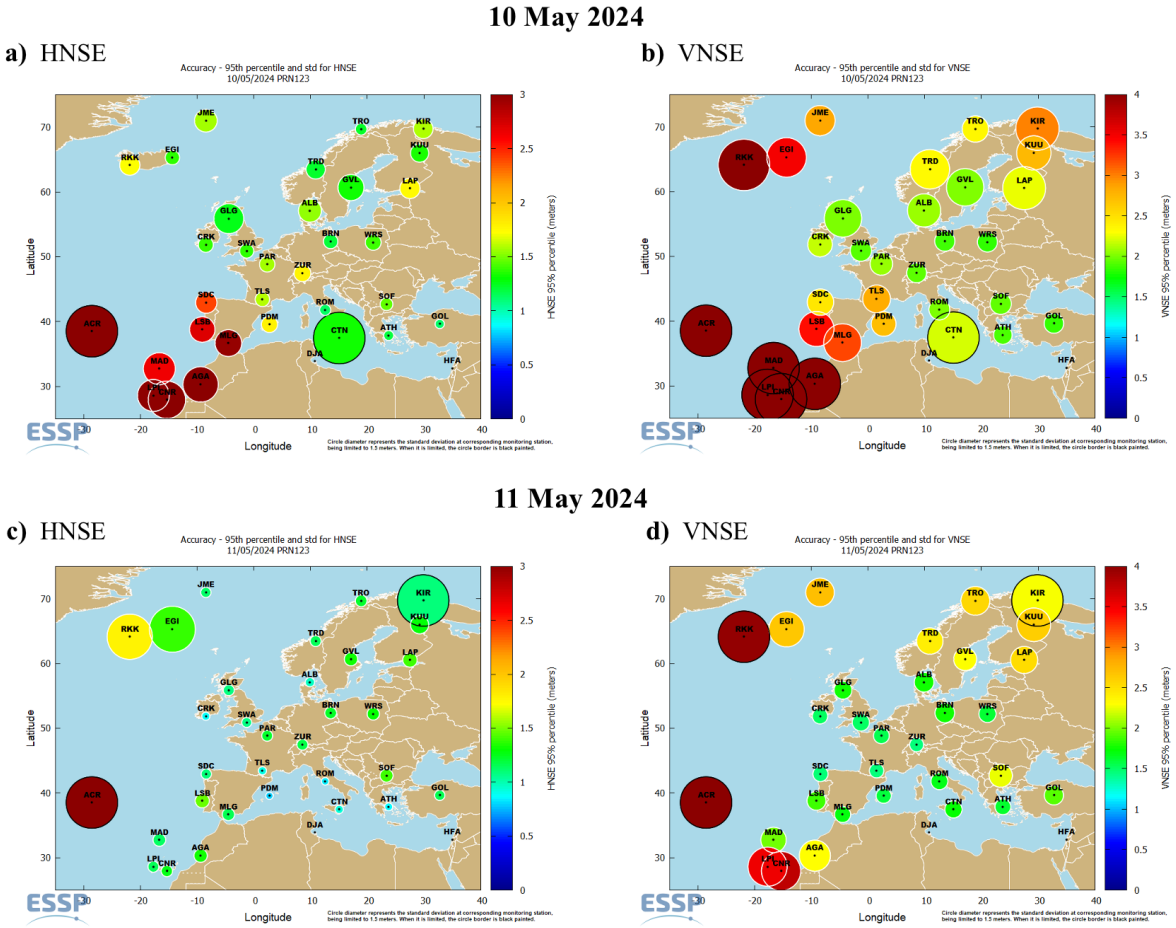

Figure 10. EGNOS performance summary plot with daily Horizontal and Vertical Navigation System Errors (HNSE and VNSE, respectively) on (top) 10 May and (bottom) 11 May 2024. Circle diameter indicates the error's standard deviation at corresponding monitoring station, being limited to 1.5 meters; when it is limited, the circle is black.

DJA (34.03°N; 10.58°E), located in Djerba, Tunisia, close to Lampedusa station, and HFA (32.78°N; 35.02°E), located in Haifa, Israel, close to Turkey. So, for the October 2024 storm, the degradation effects were observed not only near the Iberian Peninsula and the Atlantic Ocean, but also more eastward over the central and eastern Mediterranean areas. This wide area (more than 60° in east-west direction) of EGNOS performance degradation is consistent with localization of storm-induced EPBs and plasma irregularities signatures detected in ground-based GNSS ROTI, in-situ plasma density measurements, and ionosondes data.

5. Discussion

The prominent feature of this response was the formation of the storm-induced super plasma bubbles, which spread widely from equatorial to mid-latitudes in the European/African sector during the early stage of both storms. Signatures of these structures were detected by various ground-based and satellite-based measurements.

In Fig. 12, we wanted to illustrate the potential of the integrated data analysis for the specific time window of ~21-22 UT on 10 May 2024 during the first geomagnetic storm event. The idea was to superimpose the ground-based GNSS ROTI data with the COSMIC-2 satellite overpasses. But that period was particularly advantageous because supplementary observations from the GOLD and Swarm-B satellites were also available here. The NASA GOLD imager is hosted onboard a geostationary satellite over the American sector (47.5°W longitude), and it measures the Earth's far ultraviolet (UV) airglow progressively scanning the equatorial region from western Africa to the American sector (Eastes et al., 2017). GOLD provides night-time images of atomic oxygen 135.6 nm emissions; since the emission

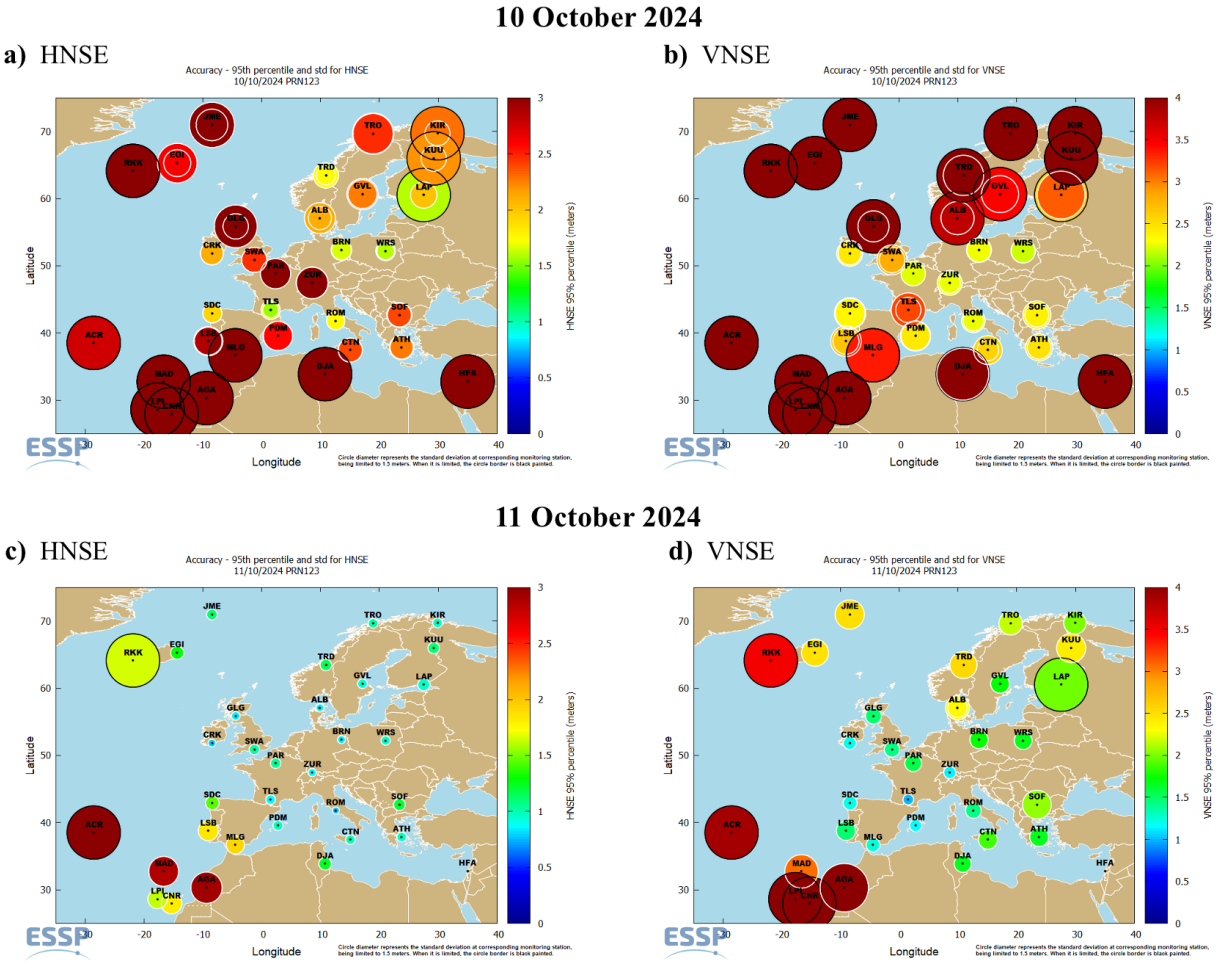

Figure 11. The same as Fig. 10 but for 10-11 October 2024.

is proportional to the square of the ionospheric plasma density, the brightness is indicative of the ionospheric peak plasma density near the F layer maximum (assumed to be near 300 km altitude). GOLD is regularly spotting EPB signatures in the form of elongated plasma density depletions in the night-time UV images (Eastes et al., 2019). Figure 12a shows the GOLD night-time 135.6 nm image for 21.8 UT on 10 May 2024 that corresponds to the western African/Atlantic sector. Two bright bands at both sides from the equator near 30°N and 20°S indicate the position of two EIA crests. A dark area over the magnetic equator shows a depleted region corresponding to the EIA trough. In GOLD images, EPB plasma depletion signatures are associated with the appearance of dark, narrow stripes elongated between two crests of the evening-time EIA. This GOLD image depicts the presence of several EPB structures indented into and even through the EIA crests up to 30°-35°N and 15°-20°S over western Africa and the Atlantic Ocean near 20°W-0°E longitudes. In the Northern Hemisphere, these EPBs exhibit a clear westward tilt. It is important to note that the observed EPB signatures in this GOLD image bore a striking resemblance to extreme EPBs developed during the 23 April 2023 geomagnetic storm that also reached mid-latitudes up to 36° MLAT exactly in this region (e.g. Karan et al., 2024b; Aa et al., 2024b; Zakharenkova et al., 2025c).

The ground-based GNSS ROTI map in Fig. 12b shows a good correspondence of the areas affected by intense irregularities (red color) and EPB locations depicted in GOLD image (Fig. 12a) over western Africa with their latitudinal stretch between 30°-35°N and 20°S, as well as their western tilt in the Northern Hemisphere near northern Africa and the Iberian Peninsula. The map in Fig. 12b also illustrates the location of satellite tracks crossing this sector, specifically two south-north tracks of Swarm-B satellite (magenta lines) and three near-equatorial tracks of COSMIC-2 satellites. It was fortunate that one of the Swarm satellites passed through this longitudinal sector during the time interval when the storm-induced EPBs developed here. The Swarm mission consists of three satellites, two satellites (Swarm-A and Swarm-C) operate in a tandem at ~475-km altitude (as of May 2024), and the third one (Swarm-B) flies at ~515 km altitude. On 10 May 2024, the descending/ascending nodes for Swarm-A/Swarm-C

and Swarm-B occurred at approximately 19.1/7.1 LT and 11.0/23.0 LT, respectively. Therefore, the tandem's LT was just before the post-sunset EPB developed, whereas the evening orbit (~23 LT) of Swarm-B was several hours after the post-sunset EPB had formed. The Swarm-B passed across the African sector at ~16°E longitude at 21.8 UT and at ~7.5°W at 23.5 UT on 10 May 2024. Figure 12c shows in situ electron density measurements along these two orbits with magenta lines for the storm day and the blue lines for previous quiet days as a reference. The Swarm-B crossing over central Africa along ~16°E longitude detected a huge plasma density depletion near the equator, spanning more than 20° in latitude between 27°N and 7°S, with electron density in the EIA trough dropped to very low levels (below 10^4 el/cm^3) over a wide area between 20°N and 5°N in latitude. The observed effects are consistent with the plasma "bite-out" phenomenon – an extensive equatorial plasma density hole created by intense storm-driven upward plasma drifts, with very steep boundaries and a density drop by 2-3 order of magnitude. Such dramatic decrease seen in the satellite-based in situ plasma density measurements is caused by the equatorial F layer rising to altitudes well above the satellite orbit (here, ~515 km). At ~23.5 UT on 10 May 2024, the next Swarm-B crossing over western Africa along ~7.5°W longitude observed even larger plasma bite-out, spanning between 27°N and 7°S latitudes with the consistently low electron density floor (below 10^4 el/cm^3) inside the EIA trough, and several significant density depletions shifted from this plasma bite out as far as ~32°N and ~10°S. Comparison of the storm-time observations with the quiet-time reference (blue curves) for the previous day demonstrates how strong these plasma bite-outs were in terms of the density drop and the latitudinal range affected. Several COSMIC-2 satellites crossed this region from west to east at ~530 km orbit altitude, quite similar to the Swarm-B orbit altitude. Figure 12d shows the corresponding in situ plasma density measurements along these COSMIC-2 orbit tracks. C2E5 satellite (orange line) passed over northern Africa at ~15° north from the magnetic equator, it encountered multiple plasma density depletions over a broad range of longitudes between 20°W and 20°E. Satellites C2E3 (green curve) and C2E6 (brown curve) crossed the equatorial region and the magnetic equator over western Africa, both of them observed a very broad plasma density hole, similar to Swarm-B plasma bite-out but in the longitudinal

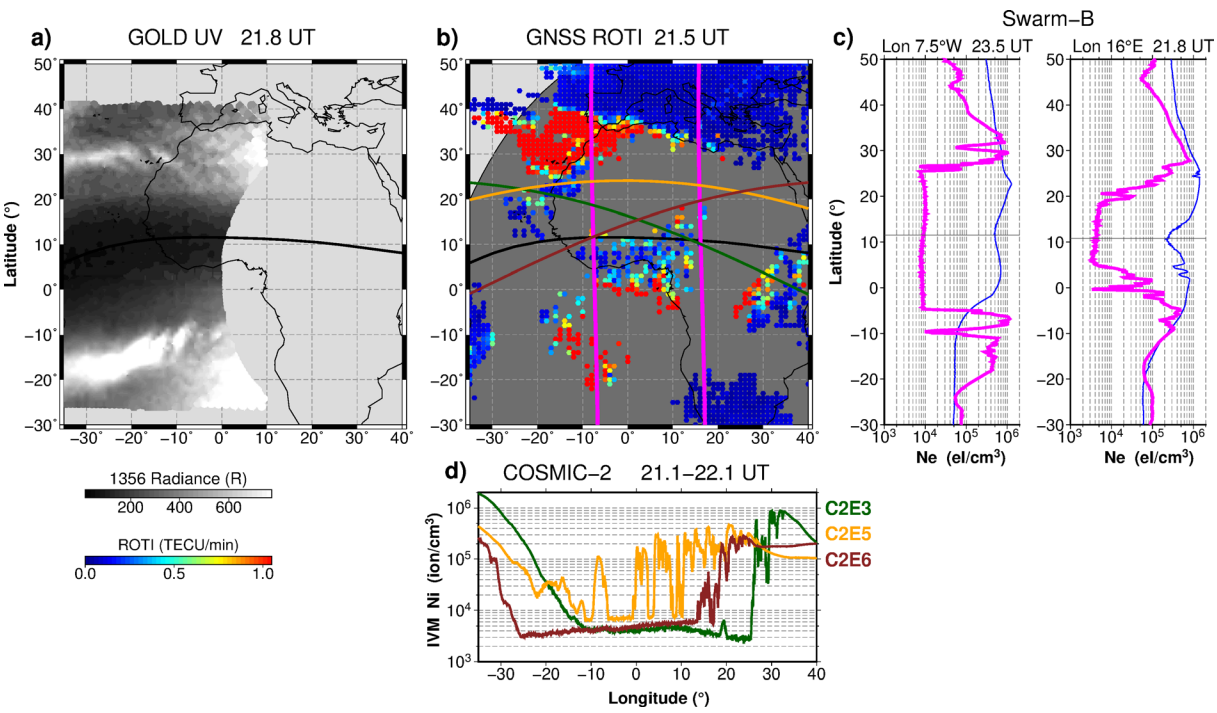

Figure 12. Consolidated plot with ground-based and satellite observations: (a) GOLD UV image for 21.8 UT on 10 May 2024; (b) GNSS ROTI map for 21.5 UT on 10 May 2024 with superimposed COSMIC-2 and Swarm-B overpasses; (c) corresponding in situ electron density (Ne) variations along two Swarm-B overpasses at 16°E and 7.5°W longitudes plotted as a function of geographical latitude, magenta curve shows Ne measurements on 10 May 2024, the thin blue curve shows Ne measurements on the previous quiet day of 9 May 2024; (d) corresponding in situ ion density (Ni) variations along COSMIC-2 C2E3, C2E5, and C2E6 passes during 21.1-22.1 UT on 10 May 2024 plotted as a function of geographical longitude.

range, the in situ plasma density dropped well below 10^4 ion/cm^3 and this low density area stretched more than 45° (4500 km) in longitude between 20°-25°W and 20°-25°E. The presence of the large-scale plasma bite-out over western Africa spanning more than 40° in latitude (Swarm-B) and more than 40° in longitude (COSMIC-2) suggest the significant uplift of the equatorial ionosphere above ~500 km altitude - it was observed just several hours after the May 2024 storm onset and most often such plasma bite-outs are associated with the intense storm-driven upward vertical drift ExB, which is primarily controlled by the eastward electric field.

Under geomagnetically quiet conditions, the evening rise of the equatorial ionosphere is correlated with the pre-reversal enhancement (PRE) in the zonal electric field, which generally occurs near 18-19 LT, this ionospheric uplift can produce steep upward-directed plasma density gradients in the bottomside ionosphere due to the concurrent recombination and electrodynamic effects, thereby setting the preconditions for Rayleigh-Taylor instability development (Woodman, 1970; Jayachandran et al., 1993; Fejer et al., 1999; Huang and Hairston, 2015; Bhattacharyya, 2022). Day-to-day variability in the PRE of the zonal electric field in the post-sunset equatorial ionosphere play a critical role in day-to-day variability of the occurrence of quiet-time EPB. Geomagnetic storms alter the zonal electric field in the equatorial ionosphere, either through prompt penetration of magnetospheric electric fields into the equatorial ionosphere (PPEFs) or through the setting up of a disturbance dynamo due to changes in global thermospheric winds driven by Joule heating and particle precipitation in the high latitude ionosphere during magnetic storms. Disturbed electric fields that penetrate the equatorial ionosphere might promote or suppress the EPB occurrence. Attributed to the sudden southward turn of the IMF Bz, the PPEFs are transmitted to the equator near instantly and have a relatively short duration of ~30-60 min (Fejer and Scherliess, 1995; Kikuchi et al., 1996, 2008). However, Huang et al. (2005) reported long-lasting PPEFs (several hours) under the steady southward IMF Bz. The PPEFs (undershielding) are typically eastward on daytime (upward drift), westward at nighttime (downward drift), and being superimposed to the PRE might result in a much larger upward vertical drifts at the post-sunset sector (Fejer et al., 2008; Huang, 2023). In contrast, the disturbance dynamo electric fields (DDEFs) take a much longer time to rise, but they last longer too. The DDEFs are driven via global scale thermospheric wind circulation due to Joule heating at high latitudes (Blanc and Richmond, 1980). They develop in ~3-4 hr after the storm initiation and are long-lived. The DDEFs tend to be westward on daytime (downward drift) and eastward at nighttime (upward drift) and lead to a larger downward drift at the dusk (Fejer et al., 2008; Richmond and Roble, 1997; Huang, 2023). Thus, the occurrence of eastward PPEFs near local sunset period can support a strong upward plasma drift and generation of intense EPBs over a narrow longitudinal sector. With storm progression, long-lasting DDEFs start to dominate and support downward plasma drift near sunset thus promoting suppression of post-sunset EPBs over a wide range of longitudes that can last for many hours or even days (e.g. Carter et al., 2016). It is important that near sunset only PPEFs can substantially boost the upward drifts in the equatorial ionosphere. Therefore, PPEFs and DDEFs might be present at a dusk sector simultaneously, especially in later stages of storm development – while PPEFs would drive upward drift uplifting the equatorial ionosphere, the counterplay of DDEFs would help only to negate the PPEFs effects in this location. During the May 2024 and October 2024 geomagnetic storms, the storm-induced EPBs occurred in the post-sunset sector right after the storm's onset. That points to the primary role of eastward-directed PPEFs supporting rapid uplift of the equatorial ionosphere at the near-sunset sector, plasma bite-outs near the magnetic equator, and post-sunset EPBs extending largely towards mid-latitudes.

Furthermore, potential PPEFs effects on the equatorial ionospheric eastward electric field (EEF) were assessed using the Real-time model of the Ionospheric Electric Fields (Manoj and Maus, 2012). The model consists of a climatological model (Scherliess and Fejer, 1999) for the quiet-time variations of EEF and a transfer function model to predict the prompt penetration contribution to EEF variation, driven by real interplanetary electric field (IEF) data from NASA/OMNI (such as in Figs. 1b, 1g). Figure 13 presents model calculations of equatorial ionospheric EEF near the magnetic equator for specific longitudes (30°E, 10°E, and 5°W) in the African sector during 10-11 May 2024 and 10-11 October 2024. Each plot shows quiet-time electric field, penetration electric field, and their superposition. The quiet-time curve has two clear peaks with positive/eastward EEF, the second one corresponds to the PRE peak that typically occurs between 18 and 19 LT (highlighted by green shading on the plots). A timely occurrence of PPEFs close to the PRE peak could intensify the superposition effect, making the combination of eastward PPEFs and normal PRE much stronger in that area. Left panel of Fig. 13 illustrates model estimation results for the May 2024 storm. For 30°E longitude (Fig. 13a), the storm onset coincided with the PRE peak time near 17 UT on 10 May 2024, the superposition effect of electric fields (red curve) looks similar to normal quiet-time variation here as there were no storm-induced effects at that time yet. At longitudes further west, 10°E and 5°W, the PRE peak time shifted to a later UT (Figs. 13b-13c). The PPEF effect appeared near 18-19 UT as a peak

to 0.5-0.7 mV/m for the blue (penetration) curve in Figs. 13b-13c, which was associated to the southward IMF Bz turn at ~18 UT (geomagnetic conditions in Figs. 1b-1c). The combined effect (red curve) of PPEF and quiet EEF produced the larger EEF effect for these longitudes, up to 1.5 mV/m. The total peak occurred slightly after the PRE maximum time at 10°E longitude but slightly before the PRE maximum time at 5°W longitude – that suggests that this entire area of western Africa was well positioned to experience the combined effect of storm-time PPEFs and the normal PRE near sunset. It is clear that PPEF effects at western Africa could be stronger than those at more easterly longitudes, such as 30°E. These model estimates are in very good agreement with the observations for 10 May 2024, when storm-induced EPBs were much larger over western Africa and the adjacent Atlantic Ocean compared with the normal-sized EPBs that formed over eastern Africa. Right panel of Fig. 13 shows similar model estimation results but for the October 2024 storm. Here, the storm started at 15:14 UT, and two fast IMF Bz turns were recorded between then and ~16:30 UT on 10 October 2024. Figure 13d showed that 30°E longitude was one of the most advantageous locations to experience the combined effect of storm-time PPEFs and normal PRE around sunset time (estimated to reach up to 2 mV/m), as its PRE peak occurred just after the storm onset within that time window. At longitudes further west, 10°E and 5°W, the PRE peak time shifted to a later UT, and therefore PPEF peaks and PRE peak were not ideally aligned resulting in much smaller overall combined PPEF-PRE effect (red curve inside the green shading areas in Figs. 13e-13f). These results align well with our observations for 10 October 2024, showing that storm-induced EPBs started earlier in UT, covered all longitudes across the African sector, and they exhibited significantly larger effect over eastern Africa, thereby impacting the eastern and central Mediterranean areas stronger than their western counterparts (such as the Iberian Peninsula and adjacent Atlantics). Therefore, the presented results of the EEF empirical model support the explanation of PPEF role in development of extreme EPBs and further clarify the longitudinal differences in the areas affected by storm-induced EPBs in the European/African sector between the May and October 2024 geomagnetic storms.

It is obvious that physics-based model simulations might better explain the physical mechanisms of the observed ionospheric storm effects and separate roles of PPEF and DDEF contributions here. However, the storm-driven extreme EPBs with very high apex altitude and large latitudinal extent represent a phenomenon that is still not well understood

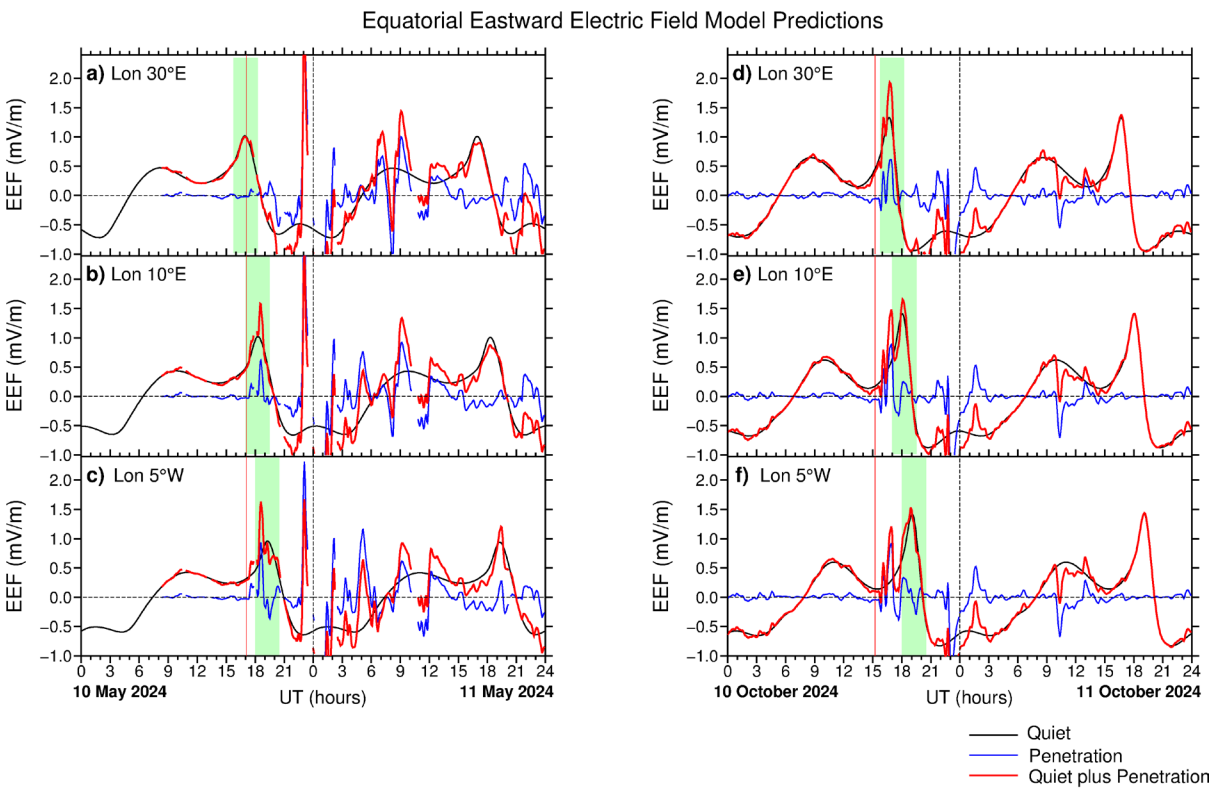

Figure 13. Model simulations of storm-time PPEF effect at 30°E, 10°E, and 5°W longitudes for 10-11 May 2024 (a-c, left column) and 10-11 October 2024 (d-f, right column). The red vertical line shows the sudden storm commencement time. Green shading area shows the normal PRE peak time at each longitude.

and challenging to simulate with stand-alone physics-based models. Only recently, in 2024, did the first successful simulation results appear in research literature, specifically in Geophysical Research Letters Journal. First, Huba and Lu (2024) used the coupled SAMI3/WACCM-X model to show that storm-induced EPBs can rise to 2000-3000 km during the recovery phase of the September 2017 storm. Here, development of post-midnight EPBs in the Asian sector was associated with storm-induced modification of the zonal and meridional winds, which caused upward E×B drift in the post-midnight sector (DDEF effects). These model simulation results are still missing an important piece of physics – PPEFs – most important for storm-driven post-sunset EPBs. Then, Wang et al. (2024) used the coupled GITM-SAMI3 model to examine direct effect of PPEFs on the development of post-sunset super-EPBs in the American sector during the September 2017 storm. The simulation results successfully reproduced formation of super-EPB structure, which extended to 40° MLAT in latitude and to 5000 km in altitude. The authors conclude that strong PPEFs played key role in leading to the poleward extension of EPBs to form super-EPBs in the post-sunset sector. More recently, Bao et al. (2025) used the MAGE (Multiscale Atmosphere Geospace Environment) model, which fully couples the magnetosphere, ionosphere, and thermosphere models, to simulate the same post-sunset super-EPBs in the American sector during the September 2017 storm. The authors specifically examined what is the primary storm-time electric field that drives the extreme density depletion in the post-sunset sector, PPEFs vs DDEFs, and their numerical experiments demonstrate that sudden enhancements in southward IMF Bz induce strong eastward PPEFs, which are the primary cause of this expanded depletion structure for the case of the September 2017 storm. These are evidently early tries at simulating the occurrence of super-EPBs, and this space weather phenomenon warrants additional observational and simulation studies for a better understanding.

Therefore, the present paper reports observational evidence of intense ionospheric irregularities, associated with storm-driven EPBs expanding largely from equatorial to mid-latitudes in the European/African longitudinal sector during the main phases of two powerful geomagnetic storms in May and October 2024. The main similarities can be summarized as following: (1) the storm-driven EPBs developed at the very early stage of the storm development, specifically just 1-3 hours after the storm onset, (2) these were post-sunset EPBs, (3) the latitudinal expansion was up to 30°-35° MLAT, (4) intense ionospheric irregularities associated with storm-driven EPBs were persisted for more than 6 hours, (5) signatures were accompanied by intense GNSS ROTI fluctuations, intense GNSS amplitude scintillation, spread-F echoes overhead the ground-based ionosondes in the affected areas. The storm onset time was similar in terms of UT closeness, however the May 2024 storm started at ~17 UT, whereas the October 2024 storm at ~15 UT. For the October 2024 storm, which started ~2 hr earlier, the area affected by largely extended EPBs covered the northern Africa, the entire Mediterranean region from Turkey to Spain, and only a small portion of the Iberian Peninsula. For the May 2024 storm, which started later in time and therefore the sunset sector was already moved further westward in the African sector, the area affected by maximal extension of super EPBs was primarily northern Africa, the western Mediterranean area, the Iberian Peninsula and the adjacent part of the Atlantic Ocean. We should emphasize that the latitudinal extent up to 36° MLAT and pronounced westward tilt of super-EPBs and ionospheric irregularities over the Atlantic Ocean during the May 2024 storm demonstrate high degree of similarities with signatures of the storm-driven extreme EPBs observed exactly in this area during the 23 April 2023 geomagnetic storm (e.g. Karan et al., 2024b; Aa et al., 2024b; Zakharenkova et al., 2025c) and during the 22 June 2015 geomagnetic storm (Cherniak and Zakharenkova, 2016; Cherniak et al., 2019). That suggests a repeatable pattern in how the storm-driven EPBs can evolve in this particular sector, which needs further investigation involving numerical simulation.

It is important to note that super-EPBs can develop and impact various longitudinal sectors within a single geomagnetic storm, given that proper conditions arise during the storm's progression. The 10-11 May 2024 geomagnetic storm started at ~17 UT on 10 May 2024 when the dusk sector went to the European/American longitudinal sector. For the European sector, the negative ionospheric storm effects were dominating during 10-11 May 2024 with a TEC reduction over mid-latitudes (e.g. Spogli et al., 2024; Pierrard et al., 2025). The striking feature was the large-scale plasma bite-out near the equator and transport of storm-driven EPBs towards low- and mid-latitudes eventually affecting the Mediterranean region in Europe too.

But several hours later after the storm onset, the spectacular intensification of the EIA was observed in the American/Atlantic longitudinal sector associated with another IMF Bz turn happened near ~22:30 UT on 10 May 2024 (see e.g. Fig. 1a) and PPEF effects (e.g. Tulasi Ram et al., 2024; Rout et al., 2025). The equatorial ionosondes in eastern Brazil recorded the rapid ionospheric F layer uplift to altitudes exceeding 1,000 km in the post-sunset hours (Fagundes et al., 2025). The triggered EIA intensification was characterized by the extensive separation of the EIA crests, expanded far away from the magnetic equator, as well as substantial widening and

deepening of the EIA trough located between the EIA crests. The formation of a huge TEC depletion/hole spanning more than 20° latitudes over the equatorial region in South America was detected in GNSS TEC maps and GOLD images for 22-23 UT on 10 May 2024 in the local post-sunset period. The Swarm-A satellite overflying the American sector just after sunset observed the EIA crest-to-crest distance reaching around 60° in latitude, indicating an exceptional development of the EIA both in magnitude and poleward expansion (Rout et al., 2025; Zakharenkova et al., 2025a). This EIA crest-to-crest separation of ~60° observed by Swarm-A on 10 May 2024 was reported to be a record-breaking, the strongest storm-time EIA/super-fountain ever detected during the entire Swarm mission era of 2013-2024 (Nayak et al., 2025). In South America, GOLD observations depicted a significant poleward shift of the southern EIA crest, its rapid evolving into a "V-shaped" structure and even merging with an enhanced aurora zone. This merging effect was first reported by Karan et al. (2024a), highlighting the disappearance of the mid-latitude ionosphere due to the previously unseen merging of the EIA crest and the aurora. We should note that for the European sector, we did not see any signatures of merging the auroral and equatorial irregularities zones, they remained clearly separated by the mid-latitude buffer zone (see ROTI maps in Figs. 2-4). This spectacular intensification of post-sunset EIA in the American sector was substantially larger than EIA intensification effects we observed several hours earlier at the early phase of storm in the European/African sector. There is no clear observational evidence that such dramatic EIA intensification creates favorable conditions for super-EPB development in the American sector or EPBs were potentially inhibited under conditions of a too strong EIA intensification with super-fast equatorial plasma uplift. There were registered only minor trace in GOLD (Karan et al., 2024a) and surprisingly low amplitude scintillation activity across the South American sector, specifically with the exception of the SAO station in southern Brazil, which showed weak-to-moderate amplitude scintillation (S4 ~0.2-0.4) on the night of 10/11 May 2024, all other stations experienced no amplitude scintillation (Zakharenkova et al., 2025d). Remarkably, during the recovery phase of the storm the super-EPBs were detected near 120°-150°E longitude in the Asian sector after 15-17 UT on 11 May 2024 (Sun et al., 2024; Suraina, 2025). These EPBs expanding to 35°-40° MLAT between Japan and Australia were generated after midnight, near the sunrise terminator, which suggests leading role of DDEFs here. Therefore, the May 2024 storm led to the development of several super-EPB events, one with post-sunset EPBs in the African sector and one with post-midnight EPBs in the Asian sector.

The October 2024 storm started at ~15 UT on 10 October 2024 and led to the formation of post-sunset super-EPBs in the European/African sector. In high degree of similarity to the May 2024 event, closer to the end of the storm's main phase, the large southward turn of IMF Bz from +20 nT to −47 nT occurred at ~22:30-22:40 UT on 10 October 2024 (see Fig. 1f), marking setting the favorable conditions for PPEFs. At that time, the sunset terminator just reached South America's western coast. Near 23:50-00:24 UT, GOLD observations revealed rapid poleward displacement of the EIA crests, formation of the large-scale depletion near the equator, and captured formation of a huge super plasma bubble structure (Zakharenkova et al., 2025b; Aa et al., 2025). The super-EPB was formed over western South America (~65°-70°W) and stretched between 20°N-45°S (±30° MLAT), much poleward than the outer edges of the EIA crests. This suggests the apex altitude of ~2500 km at the early stage of super-EPB development. The ground-based GNSS ROTI observations detected formation of the storm-time post-sunset equatorial irregularities near 65°-75°W starting at ~00 UT (19 LT), they rapidly extended poleward, reaching 30°N/55°S (~40° MLAT) during 00-03 UT on 11 October 2024. Thus, the super-EPB event formed later in the American sector was considerably more intense than the super-EPBs seen earlier in the European/African sector at the beginning stage of this storm. Therefore, the October 2024 storm led to the formation at least two super-EPB events, which were post-sunset EPBs observed in the African sector and in the American sector.

The revealed similarities and differences in the ionospheric response between the European/African and American sectors in terms of super-EPB triggering suggest that the May and October 2024 super-storms can be representative cases for further numerical simulation studies.

6. Conclusions

Solar cycle 25 officially hit its maximum in 2024, the year marked by two extreme geomagnetic storms in May and October with the SYM-H index dropping to −518 nT and −390 nT, respectively. A prominent feature of both events was the formation of the storm-induced super plasma bubbles. They occurred near the local sunset and spread widely from equatorial to mid-latitudes in the European/African longitudinal sector during the main phases of the storms. In light of the rare occurrence of super-EPBs in this area, the present study provides a multi-instrument

investigation of signatures of super-EPB structures and related ionospheric irregularities within the European/African longitudinal sector, focusing on their potential impact on Europe. The main results can be summarized as follows:

1) For both storms, the ground-based GNSS ROTI maps showed intense ionospheric irregularities extending north and south from the magnetic equator, impacting northern Africa and southern Europe, especially the Mediterranean region and the Iberian Peninsula.
2) Two storms were characterized by a high degree of similarity in time of the storm onset: ~17 UT for the 10 May 2024 storm and ~15 UT for the 10 October 2024 storm, which followed by a rapid southward turn of the IMF Bz (favorable conditions for PPEFs). If storm-induced PPEFs occur during 15-20 UT, this time interval coincides perfectly with the dusk sector progression over the African region, meaning that storm-induced electric fields might largely amplify the post-sunset EPB development in this region. Actually, storm-time EPBs started to appear over eastern Africa after ~17:30 UT on 10 May 2024 and reached ~35°N during 20-22 UT, whereas for the 10 October 2024 they first appeared over eastern Africa near 16 UT and reached their maximal latitudinal extension during 17-20 UT.
3) For the May 2024 storm, which started later in time, the area affected by maximal extension of super EPBs was primarily northern Africa, the western Mediterranean area, the Iberian Peninsula and the adjacent part of the Atlantic Ocean. For the October 2024 storm, which started ~2 hr earlier, the area affected by largely extended EPBs covered northern Africa, the entire Mediterranean region from Turkey to Spain, and only a small portion of the Iberian Peninsula. Simulation results from the Real-time model of the Ionospheric Electric Fields revealed that the most advantageous area to experience the maximal superposition effect, merging peaks in the normal PRE and additional eastward PPEFs, was located west of 10°E longitude for the May 2024 storm and near 30°E longitude for the October 2024 storm – that explains the longitude range difference in the areas of the Mediterranean region being affected by irregularities.
4) For the May 2024 storm, the observed signatures of the super-EPBs, such as their latitudinal extent reaching 35° MLAT and the pronounced westward tilt of the super-EPBs captured in GOLD UV scans over western Africa and the adjacent part of the Atlantic Ocean, were remarkably similar to the storm-induced EPBs observed over this area during the geomagnetic storms of 23 April 2023 and 22 June 2015.
5) Ground-based ionosondes in southern Europe revealed the occurrence of strong spread-F conditions associated with the appearance of storm-induced EPBs in the post-sunset sector. For the May event, the most pronounced signatures were observed at the westernmost ionosonde located in Spain (6.7°W). For the October event, the spread-F conditions in the post-sunset period were detected at all ionosondes from El Arenosillo (6.7°W) to Nicosia (33.1°E), suggesting that storm-induced irregularities extended across a much broader longitudinal range in the European/African sector.
6) From equatorial to mid-latitudes, the storm-induced EPBs cause amplitude and phase scintillation of GNSS signals for ground-based permanent receivers. Analysis of observations from available scintillation receivers from the INGV Space Weather database revealed registration of strong amplitude scintillation (S4 up to 0.5-1.0) in southern Europe during the main phase of the May and October 2024 geomagnetic storms.
7) Strong ionospheric irregularities, associated with large-scale extension of storm-induced EPBs, led to the EGNOS performance degradation in its European southern area. For both storms, the most significant degradation effects were observed over southern low-mid latitudes than those at the northern high-latitude area. For the May storm, significant degradation effects were primarily detected near the Iberian Peninsula and the Atlantic Ocean. In contrast, for the October storm, these effects largely extended eastward into the central and eastern Mediterranean areas. The areas of EGNOS performance degradation are consistent well with localization of storm-induced EPBs and plasma irregularities signatures detected in ground-based GNSS ROTI, in-situ plasma density measurements, and ionosondes data.

The occurrence of storm-induced super-EPBs that can extent from the equatorial region towards mid-latitudes is a rather rare phenomenon, which is still unpredictable and remains poorly understood, requiring further observational and modeling studies. Our comparative study demonstrated how the combined use of modern ground-based and space-borne observations can reveal some features and key characteristics of this phenomenon. Here, we precisely traced the temporal and spatial evolution of ionospheric irregularities associated with super-EPBs in the European/African sector, with a particular emphasis on their effects in Europe. We demonstrated that strong ionospheric irregularities inside EPBs can pose significant space weather threats to the operability of trans-ionospheric radio communications and navigation systems, including the operational EGNOS augmentation system in low-to-mid

latitude regions. Storm-induced plasma irregularities of equatorial origin that appear at mid-latitudes remain largely unexplored. It is important to underscore the need for continued development of monitoring infrastructure, such as operational networks of scintillation receivers in southern Europe (presently maintained through the efforts of the INGV Space Weather Monitoring Group), as well as the support of existing and future satellite missions for near-Earth plasma environment monitoring. Furthermore, it is important to better understand how these ionospheric structures affect GNSS-based systems such as EGNOS and to develop mitigation protocols for future events.

Data availability statement. GNSS data is available at SONEL (https://www.sonel.org), EUREF (https://gnss.bev.gv.at/at.gv.bev.dc/data/obs/), SOPAC (http://garner.ucsd.edu/pub/rinex/), SWEPOS (swepos.lantmateriet.se; login required), IGN France (https://rgp.ign.fr/DONNEES/diffusion/), Instituto Geografico Nacional Espana (https://datos-geodesia.ign.es), Red Extremena de Posicionamiento (https://rep-gnss.es/serv_postPro.php), ReNEP Portugal (ftp://ftp.dgterritorio.pt/), Italian Geodetic Data Archiving Facility (geodaf.mt.asi.it), TrigNET (trignet.co.za). COSMIC-2 observations are provided by COSMIC CDAAC (https://www.cosmic.ucar.edu/what-we-do/cosmic-2/data; https://doi.org/10.5065/T353-C093). Swarm observations are available through the ESA earth observation portal (https://swarm-diss.eo.esa.int/). GOLD UV data is available at the GOLD Science Data Center (https://gold.cs.ucf.edu/data/). The scintillation data is available at the INGV electronic Space Weather upper atmosphere data portal (*eSWua*, http://www.eswua.ingv.it/; Upper Atmosphere and Radio Propagation Working Group, 2020). The current and historical EGNOS status information is available through EGNOS GSC-Europa portal (https://egnos.gsc-europa.eu/services/egnos-performance-viewer). Ionograms from DIDBase digisonde network are available through GIRO (http://giro.uml.edu/; http://spase.info/SMWG/Observatory/GIRO; Reinisch and Galkin, 2011) and were processed using the SAO Explorer tool (https://ulcar.uml.edu/SAO-X/SAO-X.html). Data on the geophysical parameters data is accessible through the NASA/GSFC Space Physics Data Facility's OMNIWeb service (https://omniweb.gsfc.nasa.gov/ow.html; Papitashvili and King, 2020) and GFZ-Potsdam (https://kp.gfz-potsdam.de/en/; Matzka et al., 2021). PPEF effects were assessed using the Real-time model of Ionospheric Electric Fields (https://geomag.colorado.edu/online-calculators/real-time-model-ionospheric-electric-fields).

Acknowledgements. The authors acknowledge support of this research by the National Science Centre, Poland, Grant 2021/43/B/ST10/02604 (GNSS ROTI, satellite, and EGNOS analysis) and 2022/47/B/ST10/01766 (GNSS scintillation analysis). The authors acknowledge digisonde owner organizations and host organizations of the scintillation receivers – Italian National Agency for New Technologies, Energy and Sustainable Economic Development, Hellenic Mediterranean University, Frederick University, Nigeria National Space Research and Development Agency, and Kenya Space Agency. This publication uses data from the ionospheric observatory in Roquetes, Spain, owned and operated by the Fundació Observatori de l'Ebre. The authors acknowledge Dr. Lucilla Alfonsi and Dr. Luca Spogli for valuable discussion on INGV Space Weather Service database.

References

Aarons, J., M. Mendillo and R. Yantosca (1997). GPS phase fluctuations in the equatorial region during sunspot minimum, Radio Sci., 32, 4, 1535-1550, doi:10.1029/97RS00664.

Aarons, J. and B. Lin (1999). Development of high latitude phase fluctuations during the January 10, April 10-11, and May 15, 1997 magnetic storms, J. Atmos. Solar-Terrestrial Phys., 61, 3-4, 309-327, doi:10.1016/S1364-6826(98)00131-X.

Aa, E., W. Huang, S. Liu, A. Ridley et al. (2018). Midlatitude Plasma Bubbles Over China and Adjacent Areas During a Magnetic Storm on 8 September 2017, Sp. Weather, 16, 3, 321-331, doi:10.1002/2017SW001776.

Aa, E., S. Zou, A. Ridley, S. Zhang et al. (2019). Merging of Storm Time Midlatitude Traveling Ionospheric Disturbances and Equatorial Plasma Bubbles, Sp. Weather, 17, 2, 285-298, doi:10.1029/2018SW002101.

Aa, E., S. R. Zhang, J. Lei, F. Huang et al. (2024a). Significant Midlatitude Plasma Density Peaks and Dual-Hemisphere SED During the 10-11 May 2024 Super Geomagnetic Storm, J. Geophys. Res. Sp. Phys., 129, 11, e2024JA033360, doi:10.1029/2024JA033360.

Aa, E., S. R. Zhang, S. Zou, W. Wang et al. (2024b). Significant Midlatitude Bubble-Like Ionospheric Super-Depletion Structure (BLISS) and Dynamic Variation of Storm-Enhanced Density Plume During the 23 April 2023 Geomagnetic Storm, Sp. Weather, 22, 3, e2023SW003704, doi:10.1029/2023SW003704.

Aa, E., S. R. Zhang, A. J. Coster, M. R. Hairston et al. (2025). Super Equatorial Plasma Bubbles and Strong Longitudinal Variability During the 10-11 October 2024 Geomagnetic Storm, J. Geophys. Res. Sp. Phys., 130, e2025JA034224, doi:10.1029/2025JA034224.

Bao, S., W. Wang, V. Merkin, F. Toffoletto et al. (2025). Formation of the Bubble-Like Ionospheric Super-Depletion Structure (BLISS): MAGE Simulation of the September 2017 Storm, Geophys. Res. Lett., 52, e2025GL115945, doi:10.1029/2025GL115945.

Bhattacharyya, A. (2022). Equatorial Plasma Bubbles: A Review, Atmosphere, Basel, 13, 10, 1637, doi:10.3390/atmos13101637.

Basu, S., S. Basu, E. Mackenzie and H. E. Whitney (1985). Morphology of phase and intensity scintillations in the auroral oval and polar cap, Radio Sci., 20, 3, 347-356, doi:10.1029/RS020i003p00347.

Basu, S., Su. Basu, K. M. Groves, E. MacKenzie et al. (2005). Near-simultaneous plasma structuring in the midlatitude and equatorial ionosphere during magnetic superstorms, Geophys. Res. Lett., 32, 12, L12S05, doi:10.1029/2004GL021678.

Basu, S., Su. Basu, K. M. Groves, H. C. Yeh et al. (2001). Response of the equatorial ionosphere in the South Atlantic region to the great magnetic storm of July 15, 2000, Geophys. Res. Lett., 28, 18, 3577-3580, doi:10.1029/2001GL013259.

Blanc, M. and A. D. Richmond (1980). The ionospheric disturbance dynamo, J. Geophys. Res., 85, A4, 1669-1686, doi:10.1029/JA085iA04p01669.

Campuzano, S. A., F. Delgado-Gómez, Y. Migoya-Orué, G. Rodríguez-Caderot et al. (2023). Study of Ionosphere Irregularities over the Iberian Peninsula during Two Moderate Geomagnetic Storms Using GNSS and Ionosonde Observations, Atmosphere, 14, 2, 233, doi:10.3390/atmos14020233.

Carter, B. A., E. Yizengaw, R. Pradipta, J. M. Retterer et al. (2016). Global equatorial plasma bubble occurrence during the 2015 St. Patrick's Day storm, J. Geophys. Res. Sp. Phys., 121, 1, 894-905, doi:10.1002/2015JA022194.

Cherniak, I., A. Krankowski and I. Zakharenkova (2014). Observation of the ionospheric irregularities over the Northern Hemisphere: Methodology and service, Radio Sci., 49, 8, 653-662, doi:10.1002/2014RS005433.

Cherniak, I. and I. Zakharenkova (2016). First observations of super plasma bubbles in Europe, Geophys. Res. Lett., 43, 21, 11,137-11,145, doi:10.1002/2016GL071421.

Cherniak, I., I. Zakharenkova and S. Sokolovsky (2019). Multi-Instrumental Observation of Storm-Induced Ionospheric Plasma Bubbles at Equatorial and Middle Latitudes, J. Geophys. Res. Sp. Phys., 124, 3, 1491-1508, doi:10.1029/2018JA026309.

Cherniak, I. and I. Zakharenkova (2022). Development of the Storm-Induced Ionospheric Irregularities at Equatorial and Middle Latitudes During the 25-26 August 2018 Geomagnetic Storm, Sp. Weather, 20, 2, e2021SW002891, doi:10.1029/2021SW002891.

Cherniak, I., A. Krankowski and I. Zakharenkova (2018). ROTI Maps: a new IGS ionospheric product characterizing the ionospheric irregularities occurrence, GPS Solut., 22, 3, doi:10.1007/s10291-018-0730-1.

De Michelis, P. and G. Consolini (2025). Unveiling the Gannon Storm: How Ground-Based Magnetometers Mapped Its Global Impact, Sp. Weather, 23, 6, doi:10.1029/2025SW004350.

Eastes, R. W., W. E. McClintock, A. G. Burns, D. N. Anderson et al. (2017). The Global-Scale Observations of the Limb and Disk (GOLD) Mission, Space Sci. Rev., 212, 383-408, doi:10.1007/s11214-017-0392-2.

Eastes, R. W., S. C. Solomon, R. E. Daniell, D. N. Anderson et al. (2019). Global-Scale Observations of the Equatorial Ionization Anomaly, Geophys. Res. Lett., 46, 16, 9318-9326, doi:10.1029/2019GL084199.

EGNOS SoL SDD (2024). EGNOS Safety of Life (SoL) Service Definition Document, 3, 6, https://egnos.gsc-europa.eu/sites/default/files/documents/egnos_sol_sdd_in_force.pdf.

Fremouw, E. J., R. L. Leadabrand, R. C. Livingston et al. (1978). Early results from the DNA Wideband satellite experiment – Complex-signal scintillation, Radio Sci., 13, 1, 167-187, doi:10.1029/RS013i001p00167.

Fagundes, P. R., V. G. Pillat, J. B. Habarulema, M. T. A. H. Muella et al. (2025). Equatorial Ionization anomaly disturbances (EIA) triggered by the May 2024 solar Coronal Mass Ejection (CME): The strongest geomagnetic superstorm in the last two decades, Adv. Sp. Res., doi:10.1016/j.asr.2025.02.007.

Fejer, B. G. and L. Scherliess (1995). Time dependent response of equatorial ionospheric electric fields to magnetospheric disturbances, Geophys. Res. Lett., 22, 7, 851-854, doi:10.1029/95GL00390.

Fejer, B. G., L. Scherliess and E. R. de Paula (1999). Effects of the vertical plasma drift velocity on the generation and evolution of equatorial spread F, J. Geophys. Res. Sp. Phys., 104, A9, 19859-19869, doi:10.1029/1999ja900271.

Fejer, B. G., Jensen, J. W. and S. Y. Su (2008). Seasonal and longitudinal dependence of equatorial disturbance vertical plasma drifts, Geophys. Res. Lett, 35, 20, L20106, doi:10.1029/2008GL035584.

Gomez Socola, J., F. S. Rodrigues, J. Sousasantos, M. R. Quesada et al. (2025). On the Extraordinary L – Band Scintillation Event Observed in the American Sector During the 23-24 March 2023, Sp. Weather, 23, e2024SW004213, doi:10.1029/2024SW004213.

Gonzalez-Esparza, J. A., E. Sanchez-Garcia, M. Sergeeva, P. Corona-Romero et al. (2024). The Mother's Day Geomagnetic Storm on 10 May 2024: Aurora Observations and Low Latitude Space Weather Effects in Mexico, Sp. Weather, 22, 11, e2024SW004111, doi:10.1029/2024SW004111.

Hayakawa, H., Y. Ebihara, A. Mishev, S. Koldobskiy et al. (2025). The Solar and Geomagnetic Storms in May 2024: A Flash Data Report, Astrophys. J., 979, 49, doi:10.3847/1538-4357/ad9335.

Heelis, R. A., R. A. Stoneback, M. D. Perdue, M. D. Depew et al. (2017). Ion Velocity Measurements for the Ionospheric Connections Explorer, Space Sci. Rev., 212, 615-629, doi:10.1007/s11214-017-0383-3.

Hiyadutuje, A., D. Bilitza, T. Ojebisi, M. Kelelue et al. (2025). Assessment of the performance of the IRI's auroral oval boundary model as applied to the Mother's Day G5 storm during 10-13 May 2024, Adv. Sp. Res., 76, 12, 7241-7250, doi:10.1016/j.asr.2025.04.003.

Huba, J. D. and G. Lu (2024). Modeling Equatorial Plasma Bubbles With SAMI3/WACCM-X: September 2017 Storm, Geophys. Res. Lett., 51, 11, e2024GL109071, doi:10.1029/2024GL109071.

Huang, C. S., J. C. Foster and M. C. Kelley (2005). Long-duration penetration of the interplanetary electric field to the low-latitude ionosphere during the main phase of magnetic storms, J. Geophys. Res. Sp. Phys., 110, A11309, doi:10.1029/2005JA011202.

Huang, C. S. and M. R. Hairston (2015). The postsunset vertical plasma drift and its effects on the generation of equatorial plasma bubbles observed by the C/NOFS satellite, J. Geophys. Res. Sp. Phys., 120, 3, 2263-2275, doi:10.1002/2014JA020735.

Huang, C. S., J. C. Foster and Y. Sahai (2007). Significant depletions of the ionospheric plasma density at middle latitudes: A possible signature of equatorial spread F bubbles near the plasmapause, J. Geophys. Res. Sp. Phys., 112, 5, doi:10.1029/2007JA012307.

Huang, C. S. (2023). Identification of Penetration and Disturbance Dynamo Electric Fields and Their Effects on the Generation of Equatorial Plasma Bubbles, J. Geophys. Res. Sp. Phys., 128, e2023JA031766, doi:10.1029/2023JA031766.

Huang, C. Y., T. W. Fang, A. D. Richmond, T. J. F. Rowell et al. (2024). New Expression of the Field - Line Integrated Rayleigh-Taylor Instability Growth Rate, J. Geophys. Res. Sp. Phys., 129, e2024JA032550, doi:10.1029/2024JA032550.

Huang, F., J. Lei, S. R. Zhang, Y. Wang et al. (2024). Peculiar Nighttime Ionospheric Enhancements Over the Asian Sector During the May 2024 Superstorm, J. Geophys. Res. Sp. Phys., 129, e2024JA033350, doi:10.1029/2024JA033350.

Jayachandran, B., N. Balan, P. B. Rao, J. H. Sastri et al. (1993). HF Doppler and ionosonde observations on the onset conditions of equatorial spread F, J. Geophys. Res. Sp. Phys., 98, A8, 13741-13750, doi:10.1029/93ja00302.

Karan, D. K., C. R. Martinis, R. E. Daniell, R. W. Eastes et al. (2024a). GOLD Observations of the Merging of the Southern Crest of the Equatorial Ionization Anomaly and Aurora During the 10 and 11 May 2024 Mother's Day Super Geomagnetic Storm, Geophys. Res. Lett., 51, 15, e2024GL110632, doi:10.1029/2024GL110632.

Karan, D. K., C. R. Martinis, R. W. Eastes, R. E. Daniell et al. (2024b). GOLD Observations of Equatorial Plasma Bubbles Reaching Mid-Latitudes During the 23 April 2023 Geomagnetic Storm, Sp. Weather, 22, 6, e2023SW003847, doi:10.1029/2023SW003847.

Katamzi-Joseph, Z. T., J. B. Habarulema and M. Hernández-Pajares (2017). Midlatitude postsunset plasma bubbles observed over Europe during intense storms in April 2000 and 2001, Sp. Weather, 15, 9, 1177-1190, doi:10.1002/2017SW001674.

Kikuchi, T., H. Lühr, T. Kitamura, O. Saka and K. Schlegel (1996). Direct penetration of the polar electric field to the equator during a DP 2 event as detected by the auroral and equatorial magnetometer chains and the EISCAT radar, J. Geophys. Res., 101, A8, 17,161-17,173, doi:10.1029/96ja01299.

Kikuchi, T., K. K. Hashimoto and K. Nozaki (2008). Penetration of magnetospheric electric fields to the equator during a geomagnetic storm, J. Geophys. Res., 113, A06214, doi:10.1029/2007JA012628.

Kwak, Y., J. Kim, S. Kim, Y. Miyashita et al. (2024). Observational Overview of the May 2024 G5-Level Geomagnetic Storm: From Solar Eruptions to Terrestrial Consequences, J. Astron. Sp. Sci., 41, 3, 171-194, doi:10.5140/JASS.2024.41.3.171.

Lee, C. C. (2006), Examine the local linear growth rate of collisional Rayleigh-Taylor instability during solar maximum, J. Geophys. Res. Sp. Phys., 111, A11313, doi:10.1029/2006JA011925.

Li, G., B. Ning, B. Zhao, L. Liu et al. (2009). Characterizing the 10 November 2004 storm-time middle-latitude plasma bubble event in Southeast Asia using multi-instrument observations, J. Geophys. Res. Sp. Phys., 114, 7, A07304, doi:10.1029/2009JA014057.

Li, G., B. Ning, C. Wang, M. A. Abdu et al. (2018). Storm-Enhanced Development of Postsunset Equatorial Plasma Bubbles Around the Meridian 120°E/60°W on 7-8 September 2017, J. Geophys. Res. Sp. Phys., 123, 9, 7985-7998, doi:10.1029/2018JA025871.

Ma, G. and T. Maruyama (2006). A super bubble detected by dense GPS network at east Asian longitudes, Geophys. Res. Lett., 33, 21, L21103, doi:10.1029/2006GL027512.

Manoj, C. and S. Maus (2012). A real-time forecast service for the ionospheric equatorial zonal electric field, Space Weather, 10, 9, doi:10.1029/2012SW000825.

Martinis, C., J. Baumgardner, M. Mendillo, J. Wroten et al. (2015). The night when the auroral and equatorial ionospheres converged, J. Geophys. Res. Sp. Phys., 120, 8085-8095, doi:10.1002/2015JA021555.

Matzka, J., O. Bronkalla, K. Tornow, K. Elger et al. (2021). Geomagnetic Kp index, V. 1.0. GFZ Data Services, doi:10.5880/Kp.0001.

Nanjo, S. and K. Shiokawa (2024). Spatial structures of blue low-latitude aurora observed from Japan during the extreme geomagnetic storm of May 2024, Earth, Planets Sp., 76, 156, doi:10.1186/s40623-024-02090-9.

Nayak, C., S. Buchert, E. Yiğit, M. Ankita et al. (2025). Topside Low-Latitude Ionospheric Response to the 10-11 May 2024 Super Geomagnetic Storm as Observed by Swarm: The Strongest Storm-Time Super-Fountain During the Swarm Era?, J. Geophys. Res. Sp. Phys., 130, 3, e2024JA033340, doi:10.1029/2024JA033340.

Parker, W. E. and R. Linares (2024). Satellite drag analysis during the May 2024 Gannon geomagnetic storm, J. Spacecr. Rockets, 61, 5, 1412-1416, doi:10.2514/1.a36164.

Papitashvili, N. and J. King (2020). OMNI 1-min data, Dataset, NASA Space Physics Data Facility, doi:10.48322/45bb-8792.

Pi, X., A. J. Mannucci, U. J. Lindqwister and C. M. Ho (1997). Monitoring of global ionospheric irregularities using the worldwide GPS network, Geophys. Res. Lett., 24, 18, 2283-2286, doi:10.1029/97GL02273.

Pierrard, V., T. G. W. Verhulst, J. M. Chevalier, N. Bergeot et al. (2025). Effects of the Geomagnetic Superstorms of 10-11 May 2024 and 7-11 October 2024 on the Ionosphere and Plasmasphere, Atmosphere, 16, 299, doi:10.3390/atmos16030299.

Reinisch, B. W. and I. A. Galkin (2011). Global ionospheric radio observatory (GIRO), Earth, Planets Sp., 63, 4, 377-381, doi:10.5047/eps.2011.03.001.

Richmond, A. D. and R. G. Roble (1997). Electrodynamic coupling effects in the thermosphere/ionosphere system, Adv. Space Res., 20, 6, 1115-1124. doi:10.1016/S0273-1177(97)00754-0.

Rodrigues, F. S., J. G. Socola, A. O. Moraes, C. Martinis et al. (2021). On the Properties of and Ionospheric Conditions Associated With a Mid-Latitude Scintillation Event Observed Over Southern United States, Sp. Weather, 19, 6, e2021SW002744, doi:10.1029/2021SW002744.

Rout, D., A. Kumar, R. Singh, S. Patra et al. (2025). Evidence of Unusually Strong Equatorial Ionization Anomaly at Three Local Time Sectors During the Mother's Day Geomagnetic Storm On 10-11 May 2024, Geophys. Res. Lett., 52, 2, e2024GL111269, doi:10.1029/2024GL111269.

Singh, R., D. E. Scipión, K. Kuyeng, P. Condor et al. (2024). Ionospheric Disturbances observed over the Peruvian sector during the Mother's Day 1 Storm (G5-level) on May 10-12, 2024, J. Geophys. Res. Sp. Phys., 129, e2024JA033003, doi:10.1029/2024JA033003.

Scherliess, L. and B. G. Fejer (1999). Radar and satellite global equatorial F region vertical drift model, J. Geophys. Res., 104, A4, doi:10.1029/1999JA900025.

Sousasantos, J., J. Gomez Socola, F. S. Rodrigues, R. W. Eastes et al. (2023). Severe L-band scintillation over low-to-mid latitudes caused by an extreme equatorial plasma bubble: joint observations from ground-based monitors and GOLD, Earth, Planets Sp., 75, 41, doi:10.1186/s40623-023-01797-5.

Spogli, L., T. Alberti, P. Bagiacchi, L. Cafarella et al. (2024). The effects of the May 2024 Mother's Day superstorm over the Mediterranean sector: from data to public communication, Ann. Geophys., 67, 2, PA218, doi:10.4401/ag-9117.

Sun, W., G. Li, J. Lei, B. Zhao et al. (2023). Ionospheric Super Bubbles Near Sunset and Sunrise During the 26-28 February 2023 Geomagnetic Storm, J. Geophys. Res. Sp. Phys., 128, 11, e2023JA031864, doi:10.1029/2023JA031864.

Sun, W., G. Li, B. Zhao, S. R. Zhang et al. (2024). Midlatitude Plasma Blob-like Structures Along With Super Equatorial Plasma Bubbles During the May 2024 Great Geomagnetic Storm, Geophys. Res. Lett., 51, 21, e2024GL111638, doi:10.1029/2024GL111638.

Suraina, A., P. Rakhman, L. O. Abadi, M. M. Kilowasid et al. (2025). Pre-Sunrise Equatorial Plasma Bubble Over Indonesia During the 11 May 2024 Super Geomagnetic Storm, Earth Sp. Sci., 12, e2024EA004152, doi:10.1029/2024EA004152.

Themens, D. R., S. Elvidge, A. M. McCaffrey, P. T. Jayachandran et al. (2024). The high latitude ionospheric response to the major May 2024 geomagnetic storm: A synoptic view, Geophys. Res. Lett., 51, e2024GL111677, doi:10.1029/2024GL111677.

Tulasi Ram, S., B. Veenadhari, A. P. Dimri, J. Bulusu et al. (2024). Super-Intense Geomagnetic Storm on 10-11 May 2024: Possible Mechanisms and Impacts, Sp. Weather, 22, 12, doi:10.1029/2024SW004126.

Cesaroni, C., G. De Franceschi, C. Marcocci, E. Pica et al. (2020). Upper atmosphere physics and radiopropagation Working Group: Electronic Space Weather Upper Atmosphere Database (eSWua) – GNSS Scintillation Data, Version 1.0. Istituto Nazionale di Geofisica e Vulcanologia (INGV), doi:10.13127/ESWUA/GNSS.

Wang, Z., S. Zou, J. D. Huba and A. Ridley (2024). Development of Super Plasma Bubbles During the 7 September 2017 Geomagnetic Storm Revealed by Coupled GITM-SAMI3 Simulations, Geophys. Res. Lett., 51, 22, e2024GL112211, doi:10.1029/2024GL112211.

Weiss, J. P., W. S. Schreiner, J. J. Braun, W. Xia-Serafino et al. (2022). COSMIC-2 Mission Summary at Three Years in Orbit, Atmosphere, 13, 1409, doi:10.3390/atmos13091409.

Woodman, R. F. (1970), Vertical drift velocities and east-west electric fields at the magnetic equator, J. Geophys. Res., 75, 31, 6249-6259, doi:10.1029/JA075i031p06249.

Zakharenkova, I., E. Astafyeva and I. Cherniak (2016). GPS and GLONASS observations of large-scale traveling ionospheric disturbances during the 2015 St. Patrick's Day storm, J. Geophys. Res. Sp. Phys., 121, 12, 12, 138-12,156, doi:10.1002/2016JA023332.

Zakharenkova, I. and I. Cherniak (2020). When Plasma Streams Tie up Equatorial Plasma Irregularities with Auroral Ones, Sp. Weather, 18, 2, e2019SW002375, doi:10.1029/2019SW002375.

Zakharenkova, I. and I. Cherniak (2021). Effects of storm-induced equatorial plasma bubbles on GPS-based kinematic positioning at equatorial and middle latitudes during the September 7-8, 2017, geomagnetic storm, GPS Solut., 25, 4, doi:10.1007/s10291-021-01166-3.

Zakharenkova, I., I. Cherniak, J. J. Braun and Q. Wu (2023). Global Maps of Equatorial Plasma Bubbles Depletions Based on FORMOSAT-7/COSMIC-2 Ion Velocity Meter Plasma Density Observations, Sp. Weather, 21, 5, doi:10.1029/2023SW003438.

Zakharenkova, I., I. Cherniak, J. J. Braun, J. P. Weiss et al. (2025a). Unveiling Ionospheric Response to the May 2024 Superstorm With Low-Earth-Orbit Satellite Observations, Sp. Weather, 23, 4, e2024SW004245, doi:10.1029/2024SW004245.

Zakharenkova, I., I. Cherniak, A. Krankowski, C. Valladares et al. (2025b). On Detection of Super Equatorial Plasma Bubbles in the American Sector During the 10-11 October 2024 Geomagnetic Storm, J. Geophys. Res. Sp. Phys., 130, e2025JA033709, doi:10.1029/2025JA033709.

Zakharenkova, I., I. Cherniak, J. J. Braun, Q. Wu et al. (2025c). Multi-instrument observations of ionospheric super plasma bubbles in the European longitude sector during the 23-24 April 2023 severe geomagnetic storm, J. Sp. Weather Sp. Clim., 15, 5, doi:10.1051/swsc/2025001.

Zakharenkova, I., I. Cherniak and A. Krankowski (2025d). Large-scale ionospheric hole, unusual ionospheric gradients and irregularities observed over South America during the May 2024 geomagnetic superstorm, Adv. Sp. Res., 76, 12, 7433-7452, doi:10.1016/j.asr.2025.08.069.

***CORRESPONDING AUTHOR: Irina ZAKHARENKOVA**,
University of Warmia and Mazury, Space Radio-Diagnostic Research Center, Olsztyn, Poland
e-mail: zakharenkovai@gmail.com

© 2026 the Author(s).
Open Access. This article is licensed under a Creative Commons Attribution 3.0 International License